

# SWAS Observations of Water in Molecular Outflows

Jonathan Franklin<sup>1</sup>, Ronald L. Snell<sup>1</sup>, Michael J. Kaufman<sup>2</sup>, Gary J. Melnick<sup>3</sup>, David A. Neufeld<sup>4</sup>, David J. Hollenbach<sup>5</sup> and Edwin A. Bergin<sup>6</sup>

Received \_\_\_\_\_; accepted \_\_\_\_\_

arXiv:0711.2055v1 [astro-ph] 13 Nov 2007

---

<sup>1</sup>Department of Astronomy, LGRT 619, University of Massachusetts, 710 North Pleasant Street, Amherst, MA 01003

<sup>2</sup>Department of Physics, San Jose State University, One Washington Square, San Jose, CA 95192

<sup>3</sup>Harvard-Smithsonian Center for Astrophysics, 60 Garden Street, Cambridge MA 02138

<sup>4</sup>Department of Physics and Astronomy, Johns Hopkins University, 3400 North Charles Street, Baltimore, MD 21218

<sup>5</sup>NASA Ames Research Center, Moffett Field, CA 94035

<sup>6</sup>Department of Astronomy, University of Michigan, 825 Dennison Building, Ann Arbor, MI 48109

## ABSTRACT

We present detections of the ground-state  $1_{10} \rightarrow 1_{01}$  transition of ortho- $\text{H}_2\text{O}$  at 557 GHz in 18 molecular outflows based on data from the *Submillimeter Wave Astronomy Satellite* (SWAS). These results are combined with ground-based observations of the  $J=1-0$  transitions of  $^{12}\text{CO}$  and  $^{13}\text{CO}$  obtained at the *Five College Radio Astronomy Observatory* (FCRAO). Data from *Infrared Space Observatory* (ISO) for a subset of the outflows are also discussed. Assuming the SWAS water line emission originates from the same gas traced by CO emission, we find that the outflowing gas in most outflows has an ortho- $\text{H}_2\text{O}$  abundance relative to  $\text{H}_2$  of between about  $10^{-7}$  and  $10^{-6}$ . Analysis of the water abundance as a function of outflow velocity reveals a strong dependence. The abundance of ortho- $\text{H}_2\text{O}$  increases with velocity and at the highest outflow velocities some of the outflows have relative ortho- $\text{H}_2\text{O}$  abundances of order  $10^{-4}$ . However the mass of very high velocity gas with such elevated  $\text{H}_2\text{O}$  abundances represents less than 1% of the total outflow gas mass. The ISO LWS observations of high- $J$  rotational lines of CO and the  $179.5 \mu\text{m}$  transition of ortho- $\text{H}_2\text{O}$  provide evidence for a warmer outflow component than required to produce either the SWAS or FCRAO lines. The ISO line flux ratios can be reproduced with C-shock models with shock velocities of order  $25 \text{ km s}^{-1}$  and preshock densities of order  $10^5 \text{ cm}^{-3}$ ; these C-shocks have post-shock relative water abundances greater than  $10^{-4}$ . The mass associated with the ISO emission is also quite small compared with the total outflow mass, and is similar to that responsible for the highest velocity water emission detected by SWAS. Although the gas responsible for the ISO emission has elevated levels of water, the bulk of the outflowing gas has an abundance of ortho- $\text{H}_2\text{O}$  well below what would be expected if the gas has passed through a C-shock with shock velocities greater than  $10 \text{ km s}^{-1}$ . Gas-phase water can

be depleted in the post-shock gas due to freeze-out onto grain mantles, however the rate of freeze-out is too slow to explain our results. Therefore we believe that only a small fraction of the outflowing molecular gas has passed through shocks strong enough to fully convert the gas-phase oxygen to water. This result has implications for the acceleration mechanism of the molecular gas in these outflows.

*Subject headings:* ISM: jets and outflows — ISM: molecules — ISM: abundances — Stars: formation — Stars: winds, outflows

## 1. Introduction

Stellar winds are believed to play a pivotal role in the process of star formation. During the accretion phase of star formation, stellar winds carry away excess angular momentum that would otherwise prevent further collapse. The winds interact with and accelerate the surrounding medium, and as a result, drive molecular outflows with masses often much greater than that of the young star itself. However, the exact mechanism by which these winds interact with and accelerate the surrounding medium is still a matter of debate. A number of different models have been proposed including jets with bow shocks, jets with turbulent entrainment, and wide angle winds (Arce & Goodman 2002). The various models result in different spatial and velocity distributions of the entrained material, and therefore one approach to distinguish between the proposed models is to map the spatial and velocity structure of the outflowing molecular gas (Arce et al. 2006). Alternatively, the various acceleration mechanisms heat the gas in different ways, resulting in changes in the chemistry of the outflow as ices are sublimated and endothermic reaction pathways are opened. Thus, determinations of the chemical abundances of the outflowing molecular gas may permit us to distinguish between the various mechanisms. The review by Arce et al. (2006) suggested that molecules such as SiO, CH<sub>3</sub>OH, H<sub>2</sub>O and sulfur-bearing molecules have their abundances affected by outflow activity. For example, Bachiller et al. (2001) study of L1157 revealed significant abundance variations and suggested that the chemistry of the outflows may be useful in understanding the time evolution of outflows.

The abundance of water can be strongly affected by shocks (Kaufman & Neufeld 1996; Bergin et al. 1998) such as those predicted to exist in outflow regions. Moderate velocity shocks are capable of producing large abundances of water by releasing frozen water from dust grains and by driving all free oxygen into water through a series of gas phase chemical reactions (Kaufman & Neufeld 1996). Thus, water should be a good tracer of shocks.

The chemical reactions that produce water have been thoroughly modeled and it has been shown that the production mechanism and resulting abundance is very sensitive to temperature (Elitzur & de Jong 1978; Elitzur & Watson 1978). At gas temperatures below  $\sim 300$  K water is formed most readily through a series of ion molecule reactions that lead to the formation of  $\text{H}_3\text{O}^+$ . The dissociative recombination of  $\text{H}_3\text{O}^+$  has several possible outcomes, but has been measured in the lab to produce water in approximately 25% of the interactions (Jensen et al. 2000). This process of water production is relatively slow and modelling has shown that in a quiescent medium of density  $10^5 \text{ cm}^{-3}$  and temperature 30 K, a water abundance of roughly  $10^{-7}$  relative to molecular hydrogen is achieved after  $10^5$  years (Bergin et al. 1998).

Once the temperature of the gas rises above  $\sim 300$  K a series of endothermic neutral-neutral reactions are activated. At elevated temperatures, these reactions are very rapid compared to the ion molecule reactions, and all free oxygen is quickly driven into water (Elitzur & de Jong 1978; Elitzur & Watson 1978). Kaufman & Neufeld (1996) show that the passage of a moderate C-shock with a velocity greater than  $\sim 10 \text{ km s}^{-1}$  is able to elevate temperatures above 300 K long enough to produce greatly enhanced water abundances on the order of  $\sim 10^{-4}$  relative to  $\text{H}_2$ . More importantly, Bergin et al. (1998) showed that the enhanced water abundance persists in the post-shock gas after the gas has cooled and to significantly reduce the water abundance required  $\sim 10^5$  years even at densities as high as  $10^5 \text{ cm}^{-3}$ . Since outflow ages are typically estimated to be of order  $10^5$  years or less, any of the outflowing molecular gas that has passed through a moderate shock should be imprinted with this greatly elevated water abundance. After  $\sim 10^5$  years the abundance of water will drop as the water chemistry comes into equilibrium at the lower gas temperature and water freezes onto the cold dust grains. Evidence for this enhancement is quite apparent in the water observations of some outflows such as in Orion-BN/KL (Harwit et al. 1998; Wright et al. 2000; Melnick et al. 2000b).

The ideal nature of water as a tracer of shocked regions is countered by the difficulty of detection from ground based observatories. This problem was overcome by the successful launch of three satellites, the *Infrared Space Observatory* (ISO), the *Submillimeter Wave Astronomy Satellite* (SWAS) and *Odin*. ISO was capable of detecting a number of water transitions excited in gas warmer than about 80 K (Clegg et al. 1996) while SWAS (Melnick et al. 2000a) and *Odin* (Nordh et al. 2003; Hjalmarson et al. 2003) can observe the fundamental ortho-H<sub>2</sub>O  $1_{10} - 1_{01}$  transition at 538.3  $\mu\text{m}$ . More recently, the *Spitzer Space Telescope* has detected several mid-infrared water transitions toward NGC 2071 (Melnick et al. 2007). The fundamental transition of ortho-H<sub>2</sub>O can be readily excited at temperatures greater than about 20 K, permitting SWAS and *Odin* to trace out much cooler post-shock gas than ISO or *Spitzer*. SWAS has detected ortho-H<sub>2</sub>O emission associated with the quiescent dense molecular gas in numerous cloud cores. The relative abundance of ortho-H<sub>2</sub>O to H<sub>2</sub> in these regions was found to be on the order of  $\sim 10^{-9}$  to  $10^{-8}$  (Snell et al. 2000b), roughly 2 orders of magnitude less abundant than predicted by quiescent gas phase chemistry. The discrepancy is likely the result of water ice mantle formation on the dust grains (Bergin et al. 2000).

In this paper, we present SWAS detections of H<sub>2</sub>O emission from 18 well studied outflow regions. We selected nearby outflows (within 1 Kpc) with significant SWAS observations that we were able to obtain additional mapping data from the *Five College Radio Astronomy Observatory* (FCRAO). These outflows are driven by a mix of high and low luminosity Young Stellar Objects (YSOs). Eight of these outflows (L1448-mm, NGC 1333-SVS13, HH25mm,  $\rho$  Oph A (VLA1623), L1689N, Ser SMM1, L1157, L1228) are driven by relatively low luminosity YSOs that are in most cases individual low mass stars. The other ten sources (GL490, Orion KL, OMC 2, NGC2071, MonR2, NGC2264 D, NGC2264 C, IC 1396N, S140, Ceph A HW2) are driven by much higher luminosity YSOs that are associated with newly forming groups and clusters. We combine the SWAS H<sub>2</sub>O detections

with maps of  $^{12}\text{CO}$  and  $^{13}\text{CO}$  emission obtained at the FCRAO 14-m telescope to determine the water abundance in the outflowing gas. Additionally, we use published ISO results for six of these outflows to further expand our understanding of the SWAS results.

## 2. Observations

### 2.1. SWAS

SWAS was a NASA Small Explorer Mission that operated successfully from 1998 to 2005 (Tolls et al. 2004). SWAS simultaneously observed the  $1_{10} - 1_{01}$  transition of ortho- $\text{H}_2\text{O}$  at 556.936 GHz, the  $J = 5-4$  transition of  $^{13}\text{CO}$  at 550.926 GHz, the  $3,1-3,2$  transition of  $\text{O}_2$  at 487.249 GHz, and the  $^3P_1 - ^3P_0$  transition of  $[\text{CI}]$  at 492.161 GHz.  $\text{O}_2$  emission was not detected toward these outflows and these observations will not be discussed further. The high spectral resolution of SWAS ( $\sim 0.6 \text{ km s}^{-1}$ ) permits the kinematic separation of the outflowing gas from the ambient material within star forming regions. However, a detailed analysis of the distribution of emission in these outflows is hindered by the limited angular resolution afforded by the small aperture of SWAS. The SWAS beam is elliptical, and at the frequency of the  $\text{H}_2\text{O}$  and  $^{13}\text{CO}$  transitions has angular dimensions of  $3'.3 \times 4'.5$  and at the frequency of the  $\text{O}_2$  and  $[\text{CI}]$  transitions has angular dimensions of  $3'.5 \times 5'.0$  (Melnick et al. 2000a). Only one pointing was obtained for each source; however, in most outflows the large beam encloses the entire region of outflow activity.

Observations of these outflows were obtained by SWAS over the entire period of mission operations. The positions observed for the 18 outflows are listed in Table 1. The data was acquired by nodding the satellite alternately between the source position and a reference position relatively free of  $^{12}\text{CO}$  emission. Each position was observed over many orbits and

the total integration time on source is listed in Table 1. For each observation, an equal time was spent integrating off source toward the reference position. The on-source integration time varied from about 6 to 90 hours and thus, the rms noise level achieved varied from source to source. The shortest integration time was for OMC2, where the rms noise measured in the baseline for the H<sub>2</sub>O and <sup>13</sup>CO spectra was 0.028 K. The noise decreased as the square root of time and thus for one of the longer integration sources,  $\rho$  Oph A, an rms of 0.008 K was obtained. For the source with the longest integration time, GL490, the baselines were poorer and the rms noise obtained was only 0.010 K. Details concerning data acquisition, calibration, and reduction with SWAS are presented in Melnick et al. (2000a) and Tolls et al. (2004). The data shown in this paper are not corrected for the measured SWAS main beam efficiency of 0.90 (Melnick et al. 2000a); however, this correction has been applied in our analysis.

## 2.2. FCRAO

During the fall of 2003 and the spring of 2004, the FCRAO 14-m telescope was used to obtain maps of the <sup>12</sup>CO emission at a rest frequency of 115.271 GHz and the <sup>13</sup>CO emission at a rest frequency of 110.201 GHz. The map centers were the same positions as those used for the SWAS observations. For all observations, the 32-pixel SEQUOIA array receiver (Erickson et al. 1999) was used and data was obtained using an On-The-Fly observing technique. For each source the observations were resampled to form maps approximately 6'.0  $\times$  6'.0 in  $\Delta\alpha$  and  $\Delta\delta$  in extent with data spaced by 25". The spectrometer for each pixel was a digital autocorrelator with a bandwidth of 50 MHz and 1024 spectral channels per pixel leading to a channel spacing of approximately 0.13 km s<sup>-1</sup> for both <sup>12</sup>CO and <sup>13</sup>CO. The full-width-at-half-maximum beam size of the FCRAO telescope at the <sup>12</sup>CO frequency is 45". The spectra in these maps typically have an rms noise measured in the



baseline of 0.06 K for  $^{13}\text{CO}$  and 0.17 K for  $^{12}\text{CO}$ . The two exceptions are L1689N and  $\rho$  Oph A which transit at low elevation at the latitude of the FCRAO site and had an rms noise measured in the baseline of only 0.14 K for  $^{13}\text{CO}$  and 0.47 K for  $^{12}\text{CO}$ . The CO data shown in this paper have not been corrected for main beam efficiency, estimated to be 0.45 at the frequency of the  $^{12}\text{CO}$  line and 0.49 at the frequency of the  $^{13}\text{CO}$  line. These corrections have been applied in all subsequent analysis.

### 2.3. ISO

ISO had a much greater wavelength coverage than SWAS and was capable of measuring the far-infrared emission from a variety of ortho- and para- $\text{H}_2\text{O}$  transitions as well as a series of high-J CO emission lines (Clegg et al. 1996). Published ISO results are available for seven of the outflows in our sample: these outflows are L1448-mm (Nisini et al. 1999, 2000; Froebrich et al. 2002), NGC1333 SVS13 (Molinari et al. 2000), Ceph A HW2 (Froebrich et al. 2002), L1157 (Neufeld et al. 2000; Giannini et al. 2001), L1689N (Ceccarelli et al. 1998), HH25mm (Benedettini et al. 2000), Orion KL (Lerate et al. 2006), and Ser SMM1 (Larsson et al. 2002). Water lines were detected by ISO in all of these outflows except Ceph A HW2. The published line fluxes that we use in this paper were all obtained with the LWS instrument. With the exception of Orion KL, these spectra were obtained at relatively low spectral resolution ( $R \sim 300$ ) so they contain little velocity information. The lowest lying water line observed by ISO is the  $2_{12} - 1_{01}$  transition at 179.5  $\mu\text{m}$ . This transition originates from a higher energy level ( $E/k = 80$  K) than the transition observed by SWAS and therefore may probe a higher temperature component of water. ISO has a smaller beam than SWAS ( $\sim 75''$ ) but the resolution is still too poor to permit a detailed spatial analysis.

### 3. Summary of Observations

In Figure 1, we present the SWAS spectra of the  $1_{10} - 1_{01}$  transition of ortho- $\text{H}_2\text{O}$  for the 18 outflows in our sample. Each spectrum has only had a linear baseline removed. Seven of the outflows presented in this paper have had SWAS data published previously: NGC 2071 and L1157 (Neufeld et al. 2000), L1448-mm and IC1396N (Benedettini et al. 2002), NGC1333 SVS13 (Bergin et al. 2003), S140 and Mon R2 (Boonman et al. 2003), and L1689N (Stark et al. 2004). L1157, IC1396N and S140 have been reobserved by SWAS since the time of these publications and the complete spectra are shown in Figure 1. The initial observations of GL490 had a ripple in the baseline and so this source was reobserved. For the new observations the local oscillator setting was shifted to a value that limited the extent of useable spectrum on the blue side of the line. With the limited spectral coverage, placement of the baseline in GL490 is more questionable than in the other outflows, and therefore the extent of the outflow emission in the blue wing is very uncertain. Finally, for L1448-mm the position observed by SWAS and the center of the CO mapping at FCRAO was offset  $\sim 3'$  north-west of L1448-mm, the center of the large bipolar outflow. Thus, our observations of L1448-mm primarily probe the blueshifted lobe of the outflow. The SWAS results for  $^{13}\text{CO}$  and [CI] will be presented later in the paper.

We have obtained nearly complete CO maps of all 18 outflows. In only L1228, L1448-mm and NGC2264 D does the molecular outflow extend appreciably beyond the  $6' \times 6'$  region mapped. The CO maps of HH25mm and Ser SMM1 show obvious evidence of multiple outflows in the region mapped, and this has been noted previously (Gibb & Heaton 1993; Davis et al. 1999). The SWAS spectra, although centered on HH25mm and Ser SMM1, include emission from other outflows in these regions. Since all 18 of these outflow regions have been extensively studied and there are many published papers with outflow maps, we do not believe our CO maps provide sufficient new information to justify showing

here. A summary of the properties of these outflows and their driving sources are provided in the catalog introduced in Wu et al. (2004).

We convolved the CO data to the SWAS resolution to compare H<sub>2</sub>O and CO line profiles. However, since the outflows do not fill the SWAS beam, convolving the CO data to match the large SWAS beam substantially degraded the signal to noise in the high velocity CO line wings making profile comparison difficult. So instead, we have chosen to co-average only those <sup>12</sup>CO spectra which have an integrated intensity in either the red or blue outflow wings that is at least one-half of the integrated intensity of the peak wing emission. In these same positions we have also co-averaged the <sup>13</sup>CO spectra. Both <sup>12</sup>CO and <sup>13</sup>CO spectra averaged in this manner are shown accompanying the water spectra in Figure 1. It is worth noting a few features in the averaged CO spectra. First, in Ceph A HW2 there is a additional velocity feature at  $V_{lsr} = 5 \text{ km s}^{-1}$  that is unlikely related to the outflow. In GL490 and L1228 a weak negative feature appears in these spectra, suggesting that the reference positions were not free of <sup>12</sup>CO emission at all velocities. We excluded the velocity intervals associated with these features in the three sources in our subsequent analysis.

A cursory inspection of the CO and H<sub>2</sub>O line profiles reveal many similarities that suggest that the emission in these lines likely originates in the same outflow component. With the exceptions of Mon R2, NGC 2264 D, and S140, the H<sub>2</sub>O emission can be traced to a much higher outflow velocities than the CO emission. This effect is most pronounced in the low luminosity outflows, such as L1157 or HH25mm, and may be due to differences in the optical depth of these lines. The CO J=1-0 transition is intrinsically weak, and we might expect the optical depth of this line to be less than the water line. Higher rotational transitions of CO, which have larger optical depths, do reveal higher velocity emission. A good example is L1448-mm where observations of the J=2-1 transition of CO (Bachiller & Cernicharo 1990) reveal a velocity extent more similar to what is seen in the

water line. Although the detection of outflows is more difficult in the J=1-0 transition, the smaller optical depths make it ideal for deriving the outflow column density. We also find that the intensity ratio of the ortho-H<sub>2</sub>O emission to <sup>12</sup>CO emission increases with increasing outflow velocity. Later in the paper we will model these emissions, including the effects of optical depth, and test whether the observed changes in the intensity ratio is due to variations in the water abundance with velocity.

Finally we note that nearly all of the H<sub>2</sub>O spectra show evidence for self-absorption similar to that seen in <sup>12</sup>CO. The self-absorption feature is often much less evident in the co-added <sup>12</sup>CO spectra shown in Figure 1 than it is in the individual <sup>12</sup>CO spectra obtained toward the center of the outflow. The self-absorption feature seen in both H<sub>2</sub>O and <sup>12</sup>CO presumably arises due to foreground, quiescent, low-excitation gas absorbing the central part of the broad emission produced by the outflowing gas.

#### 4. Analysis and Results

To derive the water abundance from the SWAS ortho-H<sub>2</sub>O observations, we must quantify the density, temperature and column density of the outflowing molecular gas. Densities and temperatures are extremely difficult to determine in molecular outflows and few studies have attempted to measure these properties. Some results are available concerning the gas temperature in outflows and are summarized in Wu et al. (2004). However for the density, it is difficult to find any reliable estimates. In this paper we will simply assume values of temperature and density typical of star forming cores. Specifically, we set the density to  $10^5 \text{ cm}^{-3}$  and the temperature we assume varies from 30-100 K, depending on the luminosity of the driving source. For outflows associated with low-luminosity YSOs (L1448-mm, NGC 1333 SVS13, HH25mm,  $\rho$  Oph A, L1689N, Ser SMM1, L1157, L1228 and IC1396N) we assume a temperature of 30 K. For outflows

associated with more luminous YSOs ( GL490, OMC2, NGC2071, MonR2, NGC 2264 D, NGC2264 C, S140 and Ceph A HW2 ) we assume a temperature of 50 K and for Orion KL we assume a temperature of 100 K. These assumptions are an oversimplification of the complex temperature and density structure likely to be present in these outflows. A number of outflows were systematically investigated by Levreault (1988) and the range of densities and temperatures estimated for outflows in this study are consistent with our assumptions.

Higher temperature gas is present in nearly all of the outflows studied here as evidenced by the presence of shock excited optical emission (Herbig-Haro objects) as well as highly excited lines of a variety of molecular species seen at infrared and far infrared wavelengths. In particular, ISO has detected high-rotational transitions of CO and H<sub>2</sub>O. However, the bulk of the outflowing molecular gas likely has much lower gas temperatures. In our analysis we will first address the emission from the cooler gas ( $T = 30\text{-}100$  K) that we believe predominately gives rise to the emission in the lowest rotational transitions of CO. In § 4.6 we will address specifically the emission from the warmer gas within the outflows.

#### 4.1. Outflow Gas Column Density

We derive the column density of outflowing gas based on the <sup>12</sup>CO J=1-0 emission assuming the outflow gas temperature and density as described in the previous section. It is necessary to begin by identifying the velocity intervals over which emission from the outflowing gas dominates the ambient cloud emission. As our guide for setting these intervals, we have used the observed <sup>13</sup>CO spectra and defined the break in line profile shape as the division between ambient and outflow emission. The intervals so defined are given in Table 2 and illustrated in Figure 1. Based on these velocity intervals, we compute the integrated intensity of the CO emission in each map position for each outflow. The emission from the outflowing gas within the velocity interval around the quiescent cloud

velocity is excluded in our analysis; however, this velocity interval is relatively small and its exclusion will not strongly affect the results.

The integrated intensity of CO can be converted to a column density, assuming that the emission is optically thin and in LTE. At the high densities assumed for the molecular outflow gas (much greater than the critical density for  $^{12}\text{CO}$ ) the assumption of LTE is extremely good. The total CO column density can be written as

$$N = 1.15 \times 10^{14} e^{5.54/T} \left( \frac{1}{3} + 0.36T \right) \int T_{mb} dv,$$

where  $T$  is the excitation temperature (which is equivalent to the gas temperature in LTE), and  $T_{mb}$  is the main beam antenna temperature (antenna temperature corrected by the main beam efficiency) of the  $J=1-0$  transition of CO.

Although our assumption of LTE is likely valid, we have no reason to believe that the observed high velocity  $^{12}\text{CO}$  emission is optically thin. Our simultaneous observations of the  $^{13}\text{CO}$  emission from the outflows enable us to test this thin assumption and, if necessary, correct for any optical depth effect. We estimate the optical depth of this gas by comparing the observed ratio of  $^{12}\text{CO}/^{13}\text{CO}$  emission to the assumed local interstellar medium ratio of 65 (Langer & Penzias 1990). Assuming equal excitation temperatures for  $^{12}\text{CO}$  and  $^{13}\text{CO}$ , the relation between the observed isotopic line ratio,  $R$ , and the optical depth can be written as

$$R = \frac{1 - e^{-\tau}}{1 - e^{-\tau/65}},$$

where  $\tau$  is the optical depth of the  $^{12}\text{CO}$  emission. If we further assume that the  $^{13}\text{CO}$  emission in the high velocity gas is optically thin ( $\tau/65 \ll 1$ ) then the ratio becomes

$$R \approx \frac{65}{\tau} (1 - e^{-\tau}).$$

We then apply a correction to the column densities derived assuming the emission is optically thin, and the corrected column density is then simply

$$N_{thick} = N_{thin} \frac{\tau}{1 - e^{-\tau}} \approx N_{thin} \frac{65}{R}.$$

The sensitivity of our  $^{13}\text{CO}$  maps is insufficient to detect high velocity gas in individual spectra. Because of the limited angular extent of the outflows, if we average over the entire map or even over the SWAS beam, we severely reduce the outflow signal in the averaged spectrum. Therefore, we have averaged only those spectra that show evidence of the outflow in  $^{12}\text{CO}$  emission, following the method used to construct the  $^{12}\text{CO}$  and  $^{13}\text{CO}$  spectra shown in Figure 1. The redshifted and blueshifted gas were considered separately, unlike the method used to produce the spectra shown in Figure 1, and only those positions with  $^{12}\text{CO}$  integrated areas greater than one-half the peak value detected for the redshifted or blueshifted outflow in that source were selected and averaged together. The  $^{13}\text{CO}$  profiles were created by averaging the same positions selected by the  $^{12}\text{CO}$  emission. The observed isotope ratio in either the redshifted or blueshifted outflow is then measured from these averaged spectra. The measured isotopic ratios are presented in Table 2. The measured value of  $R$  is typically between 20 and 30 which correspond to optical depths of 3.0 to 1.8 and to column density corrections of a factor of 3.3 to 2.2. The average optical depth correction is used to correct the optically thin derived column density throughout each outflow lobe.

#### 4.2. $^{13}\text{CO}$ J=5-4 Emission - Test of Outflow Model

The SWAS observations of the J=5-4 transition of  $^{13}\text{CO}$  can be used to test our adopted physical properties and derived gas column density of these outflows. The emission in this line originates from an upper state with an energy of  $E/k = 79$  K; thus it is particularly

sensitive to the assumed temperature in the range considered for these outflows. Significant  $^{13}\text{CO}$  J=5-4 emission was detected in seven of the outflows (Ceph A HW2, GL490, MonR2, NGC2071, Orion KL, OMC 2 and S140) all driven by luminous YSOs. For outflows associated with lower luminosity YSOs,  $^{13}\text{CO}$  J=5-4 emission was either extremely weak or not detected. This general trend is consistent with our assumption that the outflowing gas associated with more luminous YSOs is warmer than that in the lower luminosity YSOs. However, a more quantitative test of our physical model can be made.

Using the computed CO gas column density and the assumed temperature and density for the outflows, we can predict the emission in the  $^{13}\text{CO}$  J=5-4 transition at each location in the outflow where we have determined the outflow column density. As in our previous column density determination, we assume that the abundance ratio of CO to  $^{13}\text{CO}$  is 65. We convolve the map of predicted emission with the SWAS beam, and compute the predicted  $^{13}\text{CO}$  J=5-4 line flux in each of the outflows and compare that with the line flux observed by SWAS. We find that for most of the sources with significant  $^{13}\text{CO}$  J=5-4 emission that the modeled and observed line fluxes are consistent within a factor of 2. The agreement is remarkably good, since only small changes in the density and temperature can greatly affect the line flux. The most discrepant outflows were Mon R2 and GL490, where the modeled line flux was 3 to 6 times larger than that observed. In three of the outflows associated with luminous YSOs, IC1396N, NGC2264 C and NGC2264 D, there was no detectable  $^{13}\text{CO}$  J=5-4 emission; however, in all cases the non-detections are consistent with the model predictions. For the outflows associated with low luminosity YSOs, only  $\rho$  Oph A and L1689N have possible weak outflow detections in the  $^{13}\text{CO}$  J=5-4 line, and the other sources (L1448-mm, NGC1333-SVS13 SVS3, HH25mm, Ser SMM1, L1157, and L1228) were not detected. We find again that for these low-luminosity outflows with weak detections or only upper limits the results are consistent in most cases with our model. The one exception is HH25mm, where the modeled flux exceeds the  $3\sigma$  upper limit by a factor



of approximately 3 to 5. In all cases where there is poor agreement, the model predictions exceed the observed line flux suggesting that we have either overestimated the temperature or density in our outflow model.

We have used two of the most discrepant outflows, MonR2 and HH25mm, to estimate the magnitude to which we may have overestimated either the density or temperature in our outflow models. Unfortunately with only the  $^{13}\text{CO}$  J=5-4 data it is impossible to derive a unique temperature and density for the outflows, since both parameters affect the observed line flux. For these calculations we have recomputed the gas column density using the modified temperature or density and then recomputed the predicted  $^{13}\text{CO}$  J=5-4 emission. In MonR2, we have found that by reducing the temperature from 50 to 30 K we can obtain good line flux agreement. However, we can also maintain the temperature at 50 K and reduce the density by a factor of 5 and obtain good agreement. Of course the correct solution could be a combination of both a lower temperature and a lower density. Likewise in HH25mm, we can achieve good flux agreement by either lowering the temperature from 30 to 20 K or by decreasing the density by a factor of 4. Nevertheless, in most outflows the line flux agreement suggests that the temperature is probably accurate to 20% and the density accurate to within a factor of two.

### 4.3. Mass of Outflows

The mass of outflowing redshifted and blueshifted gas in each outflow can be found using our map of the CO column density and the distances given in Table 1. We have assumed a CO/H<sub>2</sub> ratio of  $1 \times 10^{-4}$  for the mass determinations which are summarized in Table 2. The statistical errors on the observed integrated intensity of  $^{12}\text{CO}$  are small, and the uncertainty in our mass estimates are dominated by the uncertainties in our assumed temperature, correction for optical depth, and CO to H<sub>2</sub> conversion. Uncertainties in

density have little impact on the mass determination, unless it is substantially lower than the value we assumed.

Our method for estimating the water abundance requires a knowledge of the spatial distribution of the column density of outflowing gas. For this analysis, which we describe in the next section, we have only included positions which have a  $3\sigma$  detection of  $^{12}\text{CO}$ . The mass estimates in Table 2 are based only on positions within the outflow with CO detections, and thus may underestimate the total outflow mass. Statistically we can provide a much better estimate of the total outflow mass by using all the positions, regardless of whether the integrated intensity is positive or negative. We have recomputed the mass of each outflow without applying a detection threshold, and find masses in the redshifted and blueshifted outflows that are at most only ten percent larger than those presented in Table 2.

#### 4.4. $\text{H}_2\text{O}$ Abundance

We first estimate the ortho- $\text{H}_2\text{O}$  abundance in the outflows assuming that the  $\text{H}_2\text{O}$  emission seen by SWAS originates in the same gas as traced by the CO J=1-0 emission. Later we will explore whether this is reasonable assumption and if there are other possibilities for its origin. The integrated intensity of the SWAS  $\text{H}_2\text{O}$  line in each outflow has been determined using the same velocity intervals that were used for CO. The observed integrated intensity and line flux for the redshifted and blueshifted emission is given in Table 2. We model the water emission using a statistical equilibrium code that uses the Large Velocity Gradient (LVG) approximation to account for radiation trapping. The LVG assumption should be a valid approximation for the observed broad-line emission from these outflows. Collisional rate coefficients are taken from Phillips et al. (1996). Since the ortho- $\text{H}_2$  and para- $\text{H}_2$  collisional rate coefficients with  $\text{H}_2\text{O}$  are different by nearly

an order of magnitude, the assumed ratio of ortho-H<sub>2</sub> to para-H<sub>2</sub> is important. We have assumed that the ratio of ortho- to para-H<sub>2</sub> is in LTE as found for the outflows studied by Neufeld et al. (2006) . Thus for our assumed gas temperatures of 30, 50 and 100 K, the ratio of ortho- to para-H<sub>2</sub> is approximately 0.03, 0.3 and 1.6, respectively. We include the five lowest levels of ortho-H<sub>2</sub>O in our calculation.

The physical inputs to our H<sub>2</sub>O model are the temperature, density, and column density distribution of the outflowing gas. We have used the same temperature and density as described earlier for computing the CO column density. The process of solving for the abundance begins by assuming a water abundance and then computing the predicted water emission at each position in the outflow. We convolve the predicted emission with the SWAS beam, and then compare with the observed integrated intensity. The abundance of ortho-H<sub>2</sub>O is then varied until we achieve agreement between model and observations. This approach is very similar to that used by Snell et al. (2000a) and has the advantage of correctly accounting for optical depth variations and beam dilution effects across the large SWAS beam based on our measured gas column density distribution. Since the input to our model is the measured CO column density, our analysis provides a direct determination of the ortho-H<sub>2</sub>O abundance relative to CO. We infer an abundance of ortho-H<sub>2</sub>O relative to H<sub>2</sub> by assuming a <sup>12</sup>CO to H<sub>2</sub> ratio of 10<sup>-4</sup>. The resulting ortho-H<sub>2</sub>O abundances relative to H<sub>2</sub> are presented in Table 2.

We have investigated the impact on the relative ortho-H<sub>2</sub>O abundance for different assumed temperatures and densities. Unless the assumed density is dramatically decreased, density uncertainties have little impact on the determination of the CO column density. However, density does have a big effect on ortho-H<sub>2</sub>O abundance. Since the water emission in these outflows is approximately in the effectively thin limit (Neufeld et al. 2000), the abundance derived will be inversely proportional to the assumed density. Thus, if we were

to assume a density a factor of two larger, the resulting ortho-H<sub>2</sub>O abundance will be a factor of two smaller. Changes in the assumed temperature, on the other hand, will effect both the derived column density of CO and ortho-H<sub>2</sub>O abundance. We have used the redshifted outflows of MonR2 and L1689N as test cases. In each case we have increased and decreased the temperature by a factor of two and recomputed the CO column density and ortho-H<sub>2</sub>O abundance. We found for these outflows that increasing the temperature by a factor of two results in a decrease in the relative abundance of ortho-H<sub>2</sub>O by a factor of 3 in Mon R2 and by a factor of 8 in L1689N. Decreasing the temperature by a factor of two results in an increase in the derived ortho-H<sub>2</sub>O abundance by a factor of 9 in Mon R2 and by a factor of 5 in L1689N. Thus, our derived ortho-H<sub>2</sub>O abundances are very sensitive to the assumed physical conditions in the outflowing gas, which is unfortunate since these conditions are very poorly known. Thus, the systematic errors introduced by our poor knowledge of the outflow density and temperature dominate over the uncertainties in the H<sub>2</sub>O line fluxes in determinations of the water abundance.

The abundance of H<sub>2</sub>O relative to H<sub>2</sub> spans a wide range of values, from 10<sup>-5</sup> to 10<sup>-8</sup>. This range of abundances is so large, we believe it is unlikely due to only uncertainties in the physical conditions and must reflect true abundance variations. We note that the results for NGC2071 and L1157 are in good agreement with the abundances reported earlier by Neufeld et al. (2000) that are also based on the SWAS data. We find the highest H<sub>2</sub>O abundances are found in Orion KL and L1157, and the lowest abundance in Mon R2. Our derived ortho-H<sub>2</sub>O abundances in nearly all of the outflows are much larger than that derived for quiescent molecular cloud gas ( $\sim 10^{-9}$ ; Snell et al. 2000b) which suggests some enhancement of the water abundance in outflows. The largest abundance derived,  $\sim 10^{-5}$  in Orion KL, is still less than one might expect if all of the free oxygen had been converted into water as is expected for a moderate shock. It is very important to remember that these abundance estimates are averages over the entire SWAS beam, and do not rule out

the possibility of much higher abundances existing over a small portion of these outflows. In fact, in the warm gas probed by ISO, the abundance of H<sub>2</sub>O is as high as  $5 \times 10^{-4}$  in the warm gas in Orion KL and L1448-mm (Harwit et al. 1998; Giannini et al. 2001). The relationship of the warm gas probed by ISO and the emission seen by SWAS will be examined in more detail in § 4.6.

#### 4.5. Velocity Dependence of H<sub>2</sub>O Abundance

The high spectral resolution of SWAS enables us to further investigate the abundance of H<sub>2</sub>O as a function of velocity. In the previous section we assumed that the ortho-H<sub>2</sub>O abundance is constant throughout the outflow. We will now investigate whether the abundance of ortho-H<sub>2</sub>O relative to <sup>12</sup>CO varies with outflow velocity.

We have divided the redshifted and blueshifted emission from the outflowing gas in CO and H<sub>2</sub>O into velocity bins, each of width 5 km s<sup>-1</sup>, continuing to higher velocities until <sup>12</sup>CO is not detected. For a velocity interval to be analyzed, at least two positions within the outflow must have significant detections of <sup>12</sup>CO emission. The integrated H<sub>2</sub>O intensity and line flux as a function of velocity are presented in Table 3 for each outflow. Optical depth corrections were considered separately for each velocity interval using the same averaged CO spectra as described before. Any interval with a non-detection of <sup>13</sup>CO was assumed to be optically thin, which is often the case at the higher velocities in the outflows. We then used the same technique as discussed above to model each of the individual velocity intervals. The results of our analysis are presented in Table 3, which includes the observed CO isotopic ratio, the mass of gas, and the ortho-H<sub>2</sub>O abundance as a function of velocity.

Our abundance analysis requires <sup>12</sup>CO detections. Although, earlier we suggested that

including only  $3\sigma$  detections had only small effect on the total outflow mass, the impact of truncation is more severe in the higher velocity bins where the signal to noise of the  $^{12}\text{CO}$  emission is relatively low. We have recomputed the mass in each velocity bin without applying a detection threshold, and found that in the most discrepant bins, which are at the highest velocities, the mass could be underestimated by a factor of 2 to 3. Thus, the ortho- $\text{H}_2\text{O}$  abundances quoted may be overestimated by a similar factor. Despite these uncertainties, we find that in every outflow the derived abundance of ortho- $\text{H}_2\text{O}$  increases steadily with increasing outflow velocity. Even outflows that did not show obvious disparate velocity extents between CO and  $\text{H}_2\text{O}$  show ortho- $\text{H}_2\text{O}$  abundance variations with velocity. Some of the most pronounced abundance variations with velocity are in the outflows driven by low-luminosity YSOs; for example in NGC1333-SVS13 the ortho- $\text{H}_2\text{O}$  abundance in both the redshifted and blueshifted high velocity gas increases by two orders of magnitude from the lowest velocity outflowing gas to the highest velocity outflowing gas. At the highest outflow velocities, the abundance of ortho- $\text{H}_2\text{O}$  relative to  $\text{H}_2$  gas can be as high as  $1 \times 10^{-4}$ , approaching values that one might expect if all of the oxygen not in CO is converted into  $\text{H}_2\text{O}$  as anticipated if the gas has recently passed through a moderate velocity shock. However, since most of the outflow mass is at relatively low outflow velocities, the mass of gas with this highly elevated ortho- $\text{H}_2\text{O}$  abundance represents less than 1% of the total mass of outflowing gas, although, it accounts for a much larger fraction of total water line flux.

#### 4.6. ISO Analysis

ISO with the LWS detected both high-J CO lines and a number of ortho- and para- $\text{H}_2\text{O}$  lines in eight of the molecular outflows in our survey. The lines observed by ISO likely arise in a much warmer gas than is responsible for the bulk of the low-J CO outflow

emission that we have modeled. For water, the lowest excitation line observed by ISO (the  $2_{12} - 1_{01}$  transition at  $179.5 \mu\text{m}$ ) has a flux in most sources more than 10 times larger than that predicted by the outflow models discussed in previous sections. Thus, the ISO water emission must be produced by a warmer, likely shock-excited component, of the outflowing gas. Many authors (Harwit et al. 1998; Ceccarelli et al. 1998; Nisini et al. 2000; Molinari et al. 2000; Benedettini et al. 2000; Giannini et al. 2001) have suggested that most of the ISO emission comes from non-dissociative C-shocks with shock velocities of order 15 to  $25 \text{ km s}^{-1}$  and pre-shock densities of order  $10^4$  to  $10^5 \text{ cm}^{-3}$ . A significant enhancement of water in these post-shocked regions is needed to explain the ISO observations. Many note that the strong [OI] emission detected in all of these outflows and the detection of [SiII] in some of the outflows, may require the presence of dissociating J-shocks. Benedettini et al. (2002) compared the water emission observed by SWAS and ISO in four outflows and suggested that warm, approximately 1000 K, gas was responsible for the ISO emission and some of the SWAS emission, however they also concluded that SWAS was also sensitive to a cooler gas component not traced by ISO.

We have used the published line fluxes for L1448-mm (Nisini et al. 1999, 2000), NGC1333-SVS13 (Molinari et al. 2000), L1157 (Giannini et al. 2001), L1689N (Ceccarelli et al. 1998), HH25mm (Benedettini et al. 2000), Ser SMM1 (Larsson et al. 2002) and Orion KL (Lerate et al. 2006) to perform a simple C-shock model analysis. We note that Froebrich et al. (2002) reported two pointings of ISO toward the Ceph A HW2 outflow; however,  $\text{H}_2\text{O}$  emission was not detected, so we have not included this source in our analysis. Our modeling is aimed at estimating the shock solid angle responsible for producing the ISO emission and whether any significant fraction of the SWAS water line flux originates in this shocked gas. In Table 4 we present the flux in the  $179.5 \mu\text{m}$  line of ortho- $\text{H}_2\text{O}$  observed by ISO for the six outflows with detected emission that were in common with our survey. In L1448-mm, NGC1333-SVS13, and L1157 multiple positions

were observed by ISO and we have combined the fluxes for positions that are within the SWAS beam. In addition to CO and H<sub>2</sub>O, ISO detected relatively strong 63  $\mu\text{m}$  [OI] emission in these outflows (Ceccarelli et al. 1998; Nisini et al. 2000; Benedettini et al. 2000; Molinari et al. 2000; Giannini et al. 2001; Larsson et al. 2002).

To analyze the ISO emission, we use the C-shock models of Kaufman & Neufeld (1996). We have integrated the line intensity contributions in the post-shock gas of these C-shock models to the point where the gas has cooled to a temperature of 50 K. At that point the gas is too cool to contribute much intensity to the observed ISO lines and the freeze out of water onto dust grains may become important, which is not included in this model. In addition, the postshock gas has become indistinguishable from the gas previously modeled. We can use the high-J CO and H<sub>2</sub>O lines in conjunction with these C-shock model results to constrain the shock velocity and pre-shock gas density.

The flux in the high-J CO lines and in the 179.5  $\mu\text{m}$  transition of ortho-H<sub>2</sub>O are used to establish the correct C-shock model. The intensity ratio of the high-J CO lines, specifically the ratio of the J=20-19 transition to J=15-14 transition, is very sensitive to the temperature of the post-shock gas, and therefore provides a constraint on the shock velocity. The ratio of the CO J=15-14 line flux to 179.5  $\mu\text{m}$  water line flux is sensitive to pre-shock density. Although these line ratios vary somewhat from outflow to outflow, all outflows require shock velocities  $\gtrsim 20 \text{ km s}^{-1}$  to produce the observed ratio of CO lines. For example the average CO line flux ratio of the J=20-19/J=15-14 transitions observed is 0.45, and this ratio requires a shock velocity of 40  $\text{km s}^{-1}$  for a pre-shock gas density of  $10^4 \text{ cm}^{-3}$  or 20  $\text{km s}^{-1}$  for a pre-shock gas density of  $10^5 \text{ cm}^{-3}$ . To reproduce the observed flux ratio of CO J=15-14 to 179.5  $\mu\text{m}$  H<sub>2</sub>O, typically about unity, requires post-shock densities of  $\gtrsim 10^5 \text{ cm}^{-3}$ . We have adopted a C-shock model with a shock velocity of 25  $\text{km s}^{-1}$  and a pre-shock density of  $10^5 \text{ cm}^{-3}$ . The column of post-shock H<sub>2</sub> gas in this C-shock model to



the point where the gas has cooled to 50 K is  $6 \times 10^{21} \text{ cm}^{-2}$  and the integrated intensity of the  $179.5 \mu\text{m}$   $\text{H}_2\text{O}$  line produced by this column of post-shock gas is  $8.1 \times 10^{-3} \text{ ergs s}^{-1} \text{ cm}^{-2} \text{ sr}^{-1}$ . The  $\text{H}_2\text{O}$  abundance relative to  $\text{H}_2$  in the post-shock gas is  $4 \times 10^{-4}$ .

Based on this adopted C-shock model we estimate the total solid angle of shock front needed to reproduce the observed line flux and consequently the total mass of shocked gas; these results are given in Table 4. With the exception of Orion KL, the angular area of these shocked regions is only  $\sim 10$  square arcseconds, much smaller than the angular area of the outflow mapped in the low-J CO lines or the SWAS and ISO beamsizes. However for Orion KL, the angular size is about 1280 square arcseconds, comparable to the angular size of the outflow mapped in the low-J rotational lines of CO (Rodriguez-Franco et al. 1999). Recently, Cernicharo et al. (2006) modeled over 70 far-infrared rotational lines of water observed by ISO with the LWS. They modeled the outflow as a  $40''$  diameter shell expanding at  $25 \text{ km s}^{-1}$  with a temperature between 80-100 K, density of  $2.5\text{-}3.5 \times 10^5 \text{ cm}^{-3}$  and a relative abundance of water of  $2\text{-}3 \times 10^{-5}$ , smaller than that derived by Harwit et al. (1998). The results of Cernicharo et al. (2006) are similar to what we quoted earlier based on the SWAS data. Unlike the other outflows, the water emission observed by ISO in Orion KL may arise from the same gas that is responsible for producing the low-J CO emission.

With exception of Orion KL, the mass of warm gas needed to reproduce the ISO observed lines is only 0.0008 to 0.005 solar masses. Our mass estimates are similar to those reported by Benedettini et al. (2002) based on a thermal model with temperatures between 600 and 1400 K. Thus, the mass of warm gas responsible for producing the ISO lines is only about 1% of the total outflowing gas mass inferred from our earlier analysis of the  $\text{J}=1\text{-}0$   $^{12}\text{CO}$  line. For Orion KL, the mass in the shell model presented by Cernicharo et al. (2006) is of order 6 solar masses, similar to our total mass estimate from the low-J CO lines.

These warm, postshock gas regions probed by ISO also produce emission in the  $538 \mu\text{m}$

line observed by SWAS. The adopted C-shock model has a flux ratio of the  $179\ \mu\text{m}/538\ \mu\text{m}$  lines of ortho- $\text{H}_2\text{O}$  of approximately 32. The observed flux ratio of these lines is summarized in Table 4. It is important to remember that the ISO observations are made in a smaller beam than SWAS ( $\sim 75''$ ), so that a single ISO observation may not detect all of the  $179\ \mu\text{m}$  emission that is contained within a SWAS beam. Even in the outflows with multiple ISO pointings, the entire SWAS beam is not fully sampled, thus the observed line flux ratios in Table 4 are only lower limits. We estimate that the fraction of the SWAS water line flux that originates in the warm, post-shock gas to be as little as 10% in some outflows to more than 50 % in others. Benedettini et al. (2002) reached a similar conclusion. It may be significant that the two outflows with the most complete ISO coverage (L1448-mm and Orion KL) have the largest line flux ratios. A significant fraction of the SWAS water line flux may be arising from the very small mass of warm post-shock gas.

#### 4.7. Abundance of [CI] in Outflows

SWAS obtained very high signal to noise spectra of [CI] toward these outflow sources. Obvious high velocity [CI] emission was detected in Mon R2, L1228, Ceph A HW2, Orion KL, and S140 and spectra of [CI] in these sources are shown in Figure 2. Although no high velocity emission was detected in L1448-mm, the baseline in this source was somewhat worse. Also in Ser SMM1, the blue wing of the [CI] line was contaminated by emission in the reference position. The presence of high velocity [CI] emission in many of these outflows was previously noted by Walker et al. (1993) and Minchin et al. (1994).

In Orion KL, the spectrum shown in Figure 2 appears to have an additional emission feature at a velocity of about  $45\ \text{km s}^{-1}$ . It is unlikely that this feature is related to the redshifted outflowing gas, as the line profile would have to be significantly different from those observed in either CO or  $\text{H}_2\text{O}$ . The line is unlikely to arise from the opposite sideband.

Since SWAS does not doppler track in real time, frequency corrections are applied to each short time segment in the data pipeline, and thus lines in the opposite sideband should not add coherently to produce such a discrete feature. Assuming this feature is in the same sideband as [CI] and originates in gas with a  $V_{LSR}$  of  $9 \text{ km s}^{-1}$ , then the line frequency is approximately 492.10 GHz. We searched the JPL line list for relatively low excitation lines of molecules known to be present in Orion and the only candidates are the  $13_{3,10}$ - $13_{2,11}$  transition of  $\text{CH}_3\text{CHO}$ -e at 492.093 GHz and the  $13_{8,6}$ - $13_{7,6}$  transition of  $\text{C}_2\text{H}_5\text{OH}$  at 492.086 GHz. The lines of  $\text{CH}_3\text{CHO}$  are extremely weak in the spectrum of Orion (Sutton et al. 1985; Ziurys and McGonagle 1993), and thus is probably an unlikely identification for the feature seen by SWAS. Ethanol, on the other hand has a number of lines detected in the 336 to 340 GHz range at several locations in Orion (Sutton et al, 1995), but the frequency of the transition is significantly lower than is needed to explain the SWAS feature. None of the previously published spectra of [CI] in Orion KL had adequate sensitivity to confirm or refute this feature.

Using the same velocity intervals as defined earlier for the redshifted and blueshifted emission in each outflow, we have computed the [CI] outflow line flux. A summary of the [CI] line flux is presented in Table 5. We note that we have included the feature seen within the redshifted emission in Orion KL as part of the integrated intensity of the outflow. Although we have [CI] detections in these velocity intervals for most of the outflow sources, in many cases the emission may be dominated by the gaussian wings of the quiescent line emission. We computed the CI abundance in an identical manner as we computed the  $\text{H}_2\text{O}$  abundance, using the same physical model for each of the outflows. The resulting CI abundance relative to  $\text{H}_2$  is summarized in Table 5.

We find that the abundance of CI relative to  $\text{H}_2$  is typically about  $1 \times 10^{-5}$ . The largest abundance of CI is found for NGC2264 D and  $\rho$  Oph A. However, in NGC2264 D it is

questionable whether the weak [CI] emission in the red or blue shifted velocity intervals is related to the outflow. Very weak ( $T_A^* \sim 0.05$  K) and very broad [CI] emission is detected toward  $\rho$  Oph A, similar to the emission profile seen in  $\text{H}_2\text{O}$ . The CI abundance in  $\rho$  Oph A is about five times larger than in the other outflow. For quiescent cloud emission the abundance of CI relative to CO is typically 0.1 to 0.5 (Zmuidzinas et al. 1988; Plume et al. 2000; Howe et al. 2000), similar to that determined for the outflowing gas if we assume a CO to  $\text{H}_2$  ratio of  $1 \times 10^{-4}$ . Thus the CI in the outflowing gas is similar in abundance to that of the ambient gas in agreement with the results of Walker et al. (1993). The [CI] spectra have insufficient signal to noise to investigate variations of the CI abundance with outflow velocity.

## 5. Discussion and Conclusions

The  $1_{10} - 1_{01}$  transition of ortho- $\text{H}_2\text{O}$  at  $538 \mu\text{m}$  has been detected by SWAS in 18 molecular outflows. The  $\text{H}_2\text{O}$  line profiles are similar to the line profiles observed for the J=1-0 transition of  $^{12}\text{CO}$  and suggest that the emission seen in both species may be produced by the same gas. If we assume that the SWAS  $\text{H}_2\text{O}$  emission arises in the same gas that makes up the bulk of the molecular outflow, we find that the outflowing gas has an ortho- $\text{H}_2\text{O}$  abundance relative to  $\text{H}_2$  typically between  $10^{-6}$  and  $10^{-7}$ . However, there are a few exceptions: most notably Orion KL and L1157 have anomalously high relative ortho- $\text{H}_2\text{O}$  abundances of about  $10^{-5}$ , and Mon R2 has an anomalously low relative abundance of about  $10^{-8}$ . The relative ortho- $\text{H}_2\text{O}$  abundances in Table 2 have substantial uncertainty that arise almost solely due to the sensitivity of the derived water abundances to the assumed temperature and density of the outflowing gas, both of which are poorly known. The  $^{13}\text{CO}$  J=5-4 observations by SWAS suggest that our physical model cannot be too much in error. and thus we believe that the abundance of water in most of these

outflows is elevated relative to that measured in quiescent cloud gas. We also derive the CI abundance in the outflowing gas, and find values that are similar to quiescent cloud material, and thus unlike water, the abundance of atomic carbon appears to be unaffected by the outflow activity.

We also analyzed the velocity dependence of H<sub>2</sub>O, and find that the abundance of ortho-H<sub>2</sub>O varies significantly with velocity. In nearly all of the outflows, we find a steady increase in the ortho-H<sub>2</sub>O abundance with increasing radial velocity of the outflowing gas. In the most striking examples (NGC 1333 SVS13 and HH25mm), the abundance of water increases by two orders of magnitude from the lowest velocity to the highest velocity outflowing gas. Nevertheless, the mass of outflowing gas with greatly elevated H<sub>2</sub>O abundance is very small, representing at most only  $\sim 1\%$  of the total outflow gas mass.

The ISO observations provide evidence for the presence of a much warmer outflow component in those outflows observed. With the exception of Orion KL, our C-shock modeling of the ISO emission suggest that this warm gas constitutes less than 1 % of the total outflow mass and arises from an extremely small fraction of the molecular outflow solid angle. However, this gas is expected to have a relative abundance of water in excess of  $10^{-4}$ . The presence of this warmer component adds an additional complexity to abundance determinations in the cooler gas. Our shock modeling, although simple, suggests that a significant fraction of the water line flux observed by SWAS could arise in this warmer gas component. Unfortunately the ISO observations did not cover the full extent of the SWAS beam nor did it have velocity resolution, so it is extremely uncertain what fraction of the SWAS line flux is associated with this warm gas probed by ISO. We estimate that for the outflows with both ISO and SWAS observations, as much as 50 % of the SWAS flux could originate in the warmer gas component. If any significant fraction of the SWAS H<sub>2</sub>O line flux arises from the warm gas, then we have overestimated the line flux from the cooler

gas traced by the low-J transitions of CO, and consequently overestimated the ortho-H<sub>2</sub>O abundance in this cool gas. Therefore our estimates of the water abundance presented in Table 2 are likely to be too large. The extent to which the abundance is overestimated is very uncertain, but if only half of the SWAS line flux is due to the warm gas this only reduces the H<sub>2</sub>O abundance by a factor of two, which is well below other uncertainties in our abundance determination. Thus, unless nearly all of the SWAS line flux is due to this small mass of warm, shocked gas, the ortho-H<sub>2</sub>O abundance in the low velocity outflowing gas is enhanced relative to that measured for quiescent cloud gas (relative abundance of only 10<sup>-9</sup> to 10<sup>-8</sup> according to Snell et al. (2000b)).

The studies by Kaufman & Neufeld (1996) and Bergin et al. (1998) demonstrated that even a mild C-shock with shock velocities greater than 10 km s<sup>-1</sup> will elevate the gas temperature to permit the efficient conversion of oxygen into water and to vaporize a large fraction of the water ice on grains. Thus, most of the oxygen, not in CO, will be rapidly converted into water resulting in relative water abundances in excess of 10<sup>-4</sup>. Bergin et al. (1998) suggested that these elevated levels of water will persist long after the gas has cooled and any enhancement of the water abundance may be present over the entire lifetime of these outflows. The relative abundance of H<sub>2</sub>O is thus a good tracer of the dynamical history of the outflowing molecular gas. Our analysis of the SWAS data rules out the possibility that most of the outflow gas has passed through a shock in excess of 10 km s<sup>-1</sup>.

The ISO and high velocity SWAS results for some outflows do indicate highly elevated water abundances in a small fraction of the outflowing gas mass that is consistent with moderate velocity C-shocks. The current observations however do not have sufficient spatial and/or velocity resolution to determine exactly how these emissions might be related. It is suggestive that since the mass associated with the ISO and high velocity SWAS H<sub>2</sub>O emission are very similar that these may arise from the same C-shock. For these outflows it

would be extremely interesting to determine the spatial and kinematic relation between the ISO emission, the high velocity SWAS emission and well-established tracers of C-shocks, such as the  $2.12 \mu\text{m}$   $\text{H}_2$  emission seen in many of these outflows such as L1448-mm (Davis & Smith 1995) and NGC1333-SVS13 (Molinari et al. 2000). Future observations with *Herschel* may help out in this regards.

Mechanisms for suppressing the  $\text{H}_2\text{O}$  abundance in the postshock gas were explored by Snell et al. (2005). The only mechanism that is probably relevant for these outflows is the freeze-out of gas-phase water onto grain mantles. This was the primary mechanism in the model of Bergin et al. (1998) for the reduction of gas-phase water in post-shock gas. The timescale for significant depletion of gas-phase water depends on the post shock density of the gas and the total grain cross-section. In the model of Bergin et al. (1998), for gas denser than  $10^6 \text{ cm}^{-3}$ , the timescale is shorter than  $10^4$  years, however at densities of  $10^4 \text{ cm}^{-3}$  the time scale is longer than  $3 \times 10^5$  years. However since outflow lifetimes are extremely poorly understood, it is possible that the freeze-out of water is an important factor. Based on the timescale for water freeze-out, Snell et al. (2005) provided a simple expression for the hydrogen column density in the post-shock gas to the point where water will be frozen onto grain mantles. This calculation uses a slightly larger grain cross-section than the numerical model of Bergin et al. (1998). Assuming a shock velocity of  $10 \text{ km s}^{-1}$  and a shock compression factor of 10, the molecular hydrogen column would be of order  $10^{21} \text{ cm}^{-2}$ . If the relative abundance of ortho- $\text{H}_2\text{O}$  in this column was as  $>10^{-4}$ , as predicted by the C-shock models, the emission from this gas would greatly exceed what SWAS observed. Unless a more efficient mechanism is found for depleting the gas-phase water in the post-shock gas, we believe that the  $\text{H}_2\text{O}$  abundance in outflows provides strong evidence that the bulk of the outflowing molecular gas was never subjected to shocks greater than  $10 \text{ km s}^{-1}$  that would convert all of gas phase oxygen to water. This result places severe restrictions on the mechanism by which the molecular gas is accelerated in

these outflows and favor mechanisms, such as turbulent entrainment, that can accelerate the gas gently. However, some enhancement of the water abundance in the bulk of the outflowing gas over that measured in quiescent cloud gas may be necessary. Slower shocks ( $< 10 \text{ km s}^{-1}$ ) could heat the gas and dust to temperatures above the water-ice evaporation temperature, but below the temperature in which the rapid neutral-neutral reactions are activated, a suggestion made by Cernicharo et al. (2006) for the water abundance measured in Orion KL..

Finally we note that strong [OI] emission at a wavelength of  $63 \mu\text{m}$  was observed by ISO in all of the outflows. Many of the papers presenting ISO outflow results suggest that the origin of the [OI] emission is in J-shocks that dissociate the molecular gas. Alternatively, the [OI] emission could arise from the same weak shocks that accelerate the bulk of the molecular gas. Future observations with *Herschel*, which has better angular and spectral resolution, may help determine the relationship between the  $\text{H}_2\text{O}$  and [OI] emissions and other shock tracers in these outflows and provide a better understanding of the evolution of the  $\text{H}_2\text{O}$  abundance in these outflows.

We acknowledge the support by NASA contract NAS5-30702 that funded SWAS and NSF grant AST 01-00793 that funds the Five College Radio Astronomy Observatory. J.F acknowledges support by the NASA Goddard Center for Astrobiology through Cooperative Agreement NNG04G155A. R.L.S., M.J.K., G.J.M., D.J.H, and E.A.B. acknowledge support of grant NNG06GB30G from NASA’s LTSA prgrams. D.A.N. acknowledge the support of grant NA65-13114 from NASA’s LTSA program.



## REFERENCES

- Arce, H. G., & Goodman, A. A. 2002, *ApJ*, 575, 928
- Arce, H. G., Sheperd, D., Gueth, F., Bachiller, R., Rosen, A., & Beuther, H. 2006, to appear in *Protostars and Planets V*
- Bachiller, R., & Cernicharo, J. 1990, *A&A*, 239, 276
- Bachiller, R., Pérez Gutiérrez, M., Kumar, M. S. N., & Tafalla, M. 2001, *A&A*, 372, 899
- Benedettini, M., et al. 2000, *A&A*, 359, 148
- Benedettini, M., Viti, S., Giannini, T., Nisini, B., Goldsmith, P. F., & Saraceno, P. 2002, *A&A*, 395, 657
- Bergin, E. A., Neufeld, D. A., & Melnick, G. J. 1998, *ApJ*, 499, 777
- Bergin, E. A., et al. 2000, *ApJ*, 539, L129
- Bergin, E. A., Kaufman, M. J., Melnick, G. J., Snell, R. L., and Howe, J. E. 2003, *ApJ*, 582, 830
- Ceccarelli, C., et al. 1998, *A&A*, 331, 372
- Boonman, A.M.S., Doty, S.D., van Dishoeck, E.F., Bergin, E.A., Melnick, G.J., Wright, C.M., & Stark, R. 2003, *A&A*, 406, 937
- Cernicharo, J., Goicoechea, J.R., Daniel, F., Lerate, M.R., Barlow, M. J., Swinyard, B. M., van Dishoeck, E.F., Lim, T.L., Viti, S., & Yates, J. 2006, *ApJ*, 649, L33
- Clegg, P. E., et al. 1996, *A&A*, 315, L38
- Davis, C. J. & Smith, M. 1995, *ApJ*, 443, L41

- Davis, C. J., Matthews, H. E., Ray, T. P., Dent, W. R. F., & Richer, J. S. 1999, MNRAS, 309, 141
- Elitzur, M., & de Jong, T. 1978, A&A, 67, 323
- Elitzur, M., & Watson, W. D. 1978, A&A, 70, 443
- Erickson, N. R., Grosslein, R. M., Erickson, R. B., & Weinweb, S., 1999, IEEE Trans. Microwave Theory and Tech., 2212
- Giannini, T., Nisini, B., & Lorenzetti, D. 2001, ApJ, 555, 40
- Gibb, A. G., & Heaton, B. D. 1993, A&A, 276, 511
- Froebrich, D., Smith, M. D., & Eislöffel, J. 2002, A&A, 385, 239
- Harwit, M., Neufeld, D. A., Melnick, G. J., & Kaufman, M. J. 1998, ApJ, 497, L105
- Hjalmarson, Å. et al. 2003, A&A, 402, 39
- Hollenbach, D., 1997, in IAU Symposium 182, Herbig-Haro Flows and the Birth of Stars, eds. B. Reipurth & C. Bertout, p181
- Howe, J. E., et al. 2000, ApJ, 539, L137
- Jensen, M. J., Bilodeau, R. C., Safvan, C. P., Seiersen, K., Andersen, L. H., Pedersen, H. B., & Heber, O. 2000, ApJ, 543, 764
- Kaufman, M. J., & Neufeld, D. A. 1996, ApJ, 456, 611
- Langer, W. D. & Penzias, A. A., 1990 ApJ, 357, 477
- Larsson, B., Liseau, R., & Men'shchikov, A. B. 2002, A&A, 386, 1055

- Lerate, M. R., Barlow, M. J., Swinyard, B. M., Goicoechea, J. R., Cernicharo, J., Grundy, T. W., Lim, T. L., Polehampton, E. T., Baluteau, J.-P., Viti, S., & Yates, J. 2006, MNRAS, 370, 597
- Levreault, R. 1988, ApJS, 67, 283
- Melnick, G. J., et al. 2000, ApJ, 539, L77
- Melnick, G. J., et al. 2000, ApJ, 539, L87
- Melnick, G.J. et al. 2007, in preparation
- Minchin, N. R., White, G. J., Stutzki, J. & Krause, D. 1994, *Å*, 291, 250
- Molinari, S., et al. 2000, ApJ, 538, 698
- Neufeld, D. A., et al. 2000, ApJ, 539, L107
- Neufeld, D.A., Melnick, G. J., Sonnentrucker, P., Bergin, E.A., Green, J.D., Kim, K.H., Watson, D.M., Forrest, W.J., & Pipher, J.L. 2006, ApJ, 649, 816
- Nisini, B., et al. 1999, A&A, 350, 529
- Nisini, B., Benedettini, M., Giannini, T., Codella, C., Lorenzetti, D., di Giorgio, A. M., & Richer, J. S. 2000, A&A, 360, 297
- Nordh, H. L. et al. 2003, A&A, 402, 21
- Phillips, T. R., Maluendes, S., & Green, S. 1996, ApJS, 107, 467
- Plume, R., et al. 2000, ApJ, 539, L133
- Rodriguez-Franco, A., Martin-Pintado, J., & Wilson, T.L. 1999, A&A, 351, 1103
- Snell, R. L., et al. 2000a, ApJ, 539, L93

Snell, R. L., et al. 2000b, ApJ, 539, L101

Snell, R. L., Hollenbach, D., Howe, J.E., Neufeld, D. A., Kaurfman, M. J., Melnick, G. J.,  
Bergin, E. A., & Wang, Z. 2005, ApJ, 620, 758

Stark, R., et al. 2004, ApJ, 608, 341

Sutton, E. C., Blake, G. A., Masson, C. R. % Phillips, T. G. 1985, ApJS, 58, 341.

Sutton, E. C., Peng, R., Danchi, W. C., Jaminet, P. A. Sandell, G., & Russell, P. G. 1995,  
ApJS, 97, 455

Tolls, V., et al. 2004, ApJS, 152, 137

Walker, C., Narayanan, G., Buttgenbach, T. H., Carlstrom, J. E., Keene, J. & Phillips, T.  
G. 1993, ApJ, 415, 672

Wright, C. M., van Dishoeck, E. F., Black, J. H., Feuchtgruber, H., Cernicharo, J.,  
González-Alfonso, & deGraauw, Th. 2000, A&A, 358, 689

Wu, Y., Wei, Y., Zhao, M., Shi, Y., Yu, Y., Qin S., & Huang, M. 2004, A&A, 426, 503

Ziurys, L. M. & McGonagle, D. 1993, ApJS, 89, 155

Zmuidzinas, J., Betz, A. L., Boreiko, R. T. & Goldhaber, D. M. 1988, ApJ, 335, 774

Table 1. Positions of Observed Outflows & SWAS Observing Times

Source	$\alpha(2000)^1$	$\delta(2000)^1$	Distance pc	$t_{int}$ hr
L1448-mm	03 25 30.5	+30 45 43	300	31.47
GL490	03 27 38.5	+58 46 58	900	89.50
NGC1333-SVS13	03 29 03.7	+31 16 03	220	29.62
Orion KL	05 35 14.5	-05 22 37	500	8.50
OMC2	05 35 27.3	-05 09 49	450	6.34
HH25mm	05 46 07.3	-00 13 40	400	48.02
NGC2071	05 47 04.1	+00 21 43	390	19.32
Mon R2	06 07 46.7	-06 22 42	950	17.55
NGC2264 D	06 41 03.9	+09 34 39	800	35.55
NGC2264 C	06 41 10.7	+09 29 07	800	11.36
$\rho$ Oph A	16 26 23.4	-24 23 02	160	59.68
L1689N	16 32 22.7	-24 28 33	120	24.12
Ser SMM1	18 29 49.6	+01 15 20	310	35.60
L1157	20 39 06.5	+68 02 14	440	55.45
L1228	20 57 13.0	+77 35 47	300	33.87
IC 1396N	21 40 42.3	+58 16 10	750	59.02
S140	22 19 17.1	+63 18 46	910	24.78
Cepheus A HW2	22 56 17.9	+62 01 50	725	17.62

<sup>1</sup>Units of right ascension are hours, minutes, and seconds, and units of declination are degrees, arcminutes, and arcseconds.

Table 2. SWAS Line Fluxes and H<sub>2</sub>O Abundances<sup>a</sup>

Source		$V_{LSR}$ Interval (km s <sup>-1</sup> )	$\int T_A^*(\text{H}_2\text{O})dv$ (K km s <sup>-1</sup> )	H <sub>2</sub> O Line Flux (10 <sup>-20</sup> W cm <sup>-2</sup> )	<sup>12</sup> CO/ <sup>13</sup> CO	Mass (M <sub>⊙</sub> )	o-H <sub>2</sub> O Abundance <sup>b</sup>
L1448-mm	Blue	-31.0 → -1.0	0.28 (0.05)	0.75 (0.13)	21.4 ( 4.0)	4.9×10 <sup>-1</sup>	1.5×10 <sup>-6</sup>
	Red	8.0 → 23.0	0.27 (0.03)	0.72 (0.09)	21.6 ( 4.0)	2.9×10 <sup>-1</sup>	3.7×10 <sup>-6</sup>
GL490	Blue	-42.0 → -17.0	0.57 (0.03)	1.51 (0.09)	19.6 ( 0.7)	1.4×10 <sup>1</sup>	1.3×10 <sup>-7</sup>
	Red	-8.0 → 22.0	0.34 (0.04)	0.90 (0.10)	27.8 ( 1.7)	1.2×10 <sup>1</sup>	9.6×10 <sup>-8</sup>
NGC1333-SVS13	Blue	-20.5 → 4.5	0.54 (0.04)	1.42 (0.11)	48.3 ( 9.3)	5.4×10 <sup>-1</sup>	1.6×10 <sup>-6</sup>
	Red	11.5 → 31.5	0.64 (0.04)	1.68 (0.10)	33.4 ( 3.1)	6.7×10 <sup>-1</sup>	1.3×10 <sup>-6</sup>
Orion KL	Blue	-35.5 → 4.5	40.5 (0.09)	106.43 (0.25)	27.6 ( 0.8)	1.2×10 <sup>1</sup>	9.3×10 <sup>-6</sup>
	Red	13.5 → 53.5	48.1 (0.09)	126.41 (0.25)	27.9 ( 0.9)	9.8	1.6×10 <sup>-5</sup>
OMC-2	Blue	-2.5 → 7.5	0.84 (0.07)	2.21 (0.17)	28.0 ( 3.5)	3.4	3.6×10 <sup>-7</sup>
	Red	13.5 → 23.5	0.82 (0.07)	2.17 (0.17)	62.1 (17.7)	1.1	8.7×10 <sup>-7</sup>
HH25mm	Blue	-6.5 → 8.5	0.36 (0.03)	0.96 (0.09)	21.0 ( 0.9)	4.4	4.2×10 <sup>-7</sup>
	Red	12.0 → 37.0	0.50 (0.04)	1.33 (0.12)	25.2 ( 1.6)	4.5	7.0×10 <sup>-7</sup>
NGC2071	Blue	-23.5 → 6.5	1.04 (0.07)	2.73 (0.17)	25.7 ( 0.8)	6.8	1.1×10 <sup>-7</sup>
	Red	12.5 → 37.5	1.73 (0.06)	4.55 (0.16)	33.4 ( 1.2)	6.9	2.1×10 <sup>-7</sup>
MonR2	Blue	-2.2 → 7.8	0.47 (0.04)	1.23 (0.10)	10.3 ( 0.1)	1.2×10 <sup>2</sup>	1.8×10 <sup>-8</sup>
	Red	13.0 → 28.0	0.59 (0.05)	1.56 (0.12)	8.6 ( 0.1)	2.6×10 <sup>2</sup>	1.3×10 <sup>-8</sup>
NGC2264 D	Blue	-9.0 → 1.0	0.13 (0.03)	0.33 (0.07)	...	1.8	1.4×10 <sup>-6</sup>
	Red	10.0 → 20.0	0.19 (0.03)	0.51 (0.07)	...	1.9	2.4×10 <sup>-6</sup>
NGC2264 C	Red	11.0 → 21.0	0.83 (0.04)	2.18 (0.11)	21.1 ( 1.1)	7.2	1.7×10 <sup>-6</sup>
ρ Oph A	Blue	-3.5 → 1.5	0.28 (0.01)	0.74 (0.04)	17.8 ( 2.7)	2.2×10 <sup>-1</sup>	9.4×10 <sup>-7</sup>
	Red	6.0 → 11.0	0.17 (0.01)	0.43 (0.04)	13.3 ( 1.1)	4.3×10 <sup>-1</sup>	3.7×10 <sup>-7</sup>
L1689N	Blue	-12.5 → 2.5	0.57 (0.05)	1.49 (0.12)	18.8 ( 2.4)	2.7×10 <sup>-1</sup>	9.4×10 <sup>-7</sup>
	Red	6.0 → 21.0	1.08 (0.05)	2.84 (0.12)	20.8 ( 3.0)	1.1×10 <sup>-1</sup>	2.9×10 <sup>-6</sup>

Table 2—Continued

Source		$V_{LSR}$ Interval (km s <sup>-1</sup> )	$\int T_A^*(\text{H}_2\text{O})dv$ (K km s <sup>-1</sup> )	H <sub>2</sub> O Line Flux (10 <sup>-20</sup> W cm <sup>-2</sup> )	<sup>12</sup> CO/ <sup>13</sup> CO	Mass (M <sub>⊙</sub> )	o-H <sub>2</sub> O Abundance <sup>b</sup>
Ser SMM1	Blue	-4.5 → 5.5	0.40 (0.02)	1.05 (0.06)	19.8 ( 1.3)	1.8	7.1×10 <sup>-7</sup>
	Red	11.0 → 21.0	0.32 (0.02)	0.83 (0.06)	20.0 ( 1.1)	2.9	3.8×10 <sup>-7</sup>
L1157	Blue	-13.5 → 1.5	0.70 (0.02)	1.84 (0.06)	28.7 ( 5.1)	4.1×10 <sup>-1</sup>	8.0×10 <sup>-6</sup>
	Red	4.0 → 29.0	0.60 (0.03)	1.58 (0.08)	...	3.2×10 <sup>-1</sup>	9.7×10 <sup>-6</sup>
L1228	Blue	-19.5 → -9.5	0.17 (0.02)	0.45 (0.06)	21.7 ( 1.3)	8.7×10 <sup>-1</sup>	5.9×10 <sup>-7</sup>
	Red	-6.0 → 4.0	0.14 (0.02)	0.38 (0.06)	20.7 ( 2.5)	5.1×10 <sup>-1</sup>	8.5×10 <sup>-7</sup>
IC1396N	Blue	-18.0 → -3.0	0.36 (0.02)	0.95 (0.06)	31.3 ( 6.0)	1.5	2.7×10 <sup>-6</sup>
	Red	4.0 → 19.0	0.33 (0.02)	0.88 (0.06)	36.2 ( 9.1)	1.2	3.2×10 <sup>-6</sup>
S140	Blue	-36.0 → -11.0	0.24 (0.04)	0.63 (0.11)	15.7 ( 0.4)	3.2×10 <sup>1</sup>	2.4×10 <sup>-8</sup>
	Red	-4.0 → 6.0	0.47 (0.03)	1.25 (0.07)	18.3 ( 0.6)	1.6×10 <sup>1</sup>	1.0×10 <sup>-7</sup>
Ceph A HW2	Blue	-35.0 → -15.0	1.34 (0.06)	3.53 (0.16)	14.8 ( 0.5)	1.8×10 <sup>1</sup>	1.9×10 <sup>-7</sup>
	Red	-6.0 → 14.0	1.27 (0.06)	3.35 (0.16)	19.0 ( 0.9)	1.7×10 <sup>1</sup>	2.0×10 <sup>-7</sup>

<sup>a</sup>The numbers in parantheses are 1- $\sigma$  statistical uncertainties on the integrated intensity, line flux and observed isotopic ratio

<sup>b</sup>o-H<sub>2</sub>O abundances relative to H<sub>2</sub> assuming a H<sub>2</sub>/CO ratio of 10<sup>4</sup>

Table 3. SWAS Line Fluxes and H<sub>2</sub>O Abundances as a Function of Velocity<sup>a</sup>

Source		$V_{LSR}$ Interval (km s <sup>-1</sup> )	$\int T_A^*(\text{H}_2\text{O})dv$ (K km s <sup>-1</sup> )	H <sub>2</sub> O Line Flux (10 <sup>-20</sup> W cm <sup>-2</sup> )	<sup>12</sup> CO/ <sup>13</sup> CO	Mass (M <sub>⊙</sub> )	o-H <sub>2</sub> O Abundance <sup>b</sup>
L1448-mm	Blue	-6.0 → -1.0	0.07 (0.02)	0.18 (0.05)	31.3 ( 9.3)	1.6×10 <sup>-1</sup>	1.2×10 <sup>-6</sup>
		-11.0 → -6.0	< 0.06	< 0.16	...	2.1×10 <sup>-2</sup>	<7.1×10 <sup>-6</sup>
		-16.0 → -11.0	0.06 (0.02)	0.16 (0.05)	...	9.7×10 <sup>-3</sup>	1.2×10 <sup>-5</sup>
		-21.0 → -16.0	0.06 (0.02)	0.16 (0.05)	...	9.4×10 <sup>-3</sup>	1.3×10 <sup>-5</sup>
		-26.0 → -21.0	< 0.06	< 0.16	...	2.6×10 <sup>-3</sup>	<4.5×10 <sup>-5</sup>
		-31.0 → -26.0	< 0.06	< 0.16	...	3.2×10 <sup>-3</sup>	<4.4×10 <sup>-5</sup>
	Red	8.0 → 13.0	0.12 (0.02)	0.31 (0.05)	36.8 ( 9.0)	1.3×10 <sup>-1</sup>	3.5×10 <sup>-6</sup>
		13.0 → 18.0	0.08 (0.02)	0.21 (0.05)	9.0 ( 2.4)	8.3×10 <sup>-2</sup>	4.3×10 <sup>-6</sup>
		18.0 → 23.0	0.08 (0.02)	0.20 (0.05)	...	4.3×10 <sup>-3</sup>	1.1×10 <sup>-4</sup>
GL490	Blue	-22.0 → -17.0	0.15 (0.01)	0.39 (0.04)	19.1 ( 0.5)	9.9	4.8×10 <sup>-8</sup>
		-27.0 → -22.0	0.11 (0.01)	0.29 (0.04)	21.2 ( 1.5)	3.1	1.1×10 <sup>-7</sup>
		-32.0 → -27.0	0.13 (0.01)	0.34 (0.04)	28.2 ( 6.7)	6.7×10 <sup>-1</sup>	5.4×10 <sup>-7</sup>
		-37.0 → -32.0	0.08 (0.01)	0.22 (0.04)	...	1.3×10 <sup>-1</sup>	1.8×10 <sup>-6</sup>
		-42.0 → -37.0	0.10 (0.01)	0.28 (0.04)	...	3.4×10 <sup>-2</sup>	8.3×10 <sup>-6</sup>
	Red	-8.0 → -3.0	0.10 (0.01)	0.26 (0.04)	24.0 ( 0.9)	8.8	3.9×10 <sup>-8</sup>
		-3.0 → 2.0	0.08 (0.01)	0.22 (0.04)	44.6 ( 7.2)	1.4	1.7×10 <sup>-7</sup>
		2.0 → 7.0	0.05 (0.01)	0.14 (0.04)	34.3 (11.3)	5.3×10 <sup>-1</sup>	2.7×10 <sup>-7</sup>
		7.0 → 12.0	< 0.04	< 0.12	...	1.6×10 <sup>-1</sup>	<7.5×10 <sup>-7</sup>
		12.0 → 17.0	0.07 (0.01)	0.18 (0.04)	...	8.3×10 <sup>-2</sup>	2.5×10 <sup>-6</sup>
17.0 → 22.0	< 0.04	< 0.12	...	2.6×10 <sup>-2</sup>	<4.5×10 <sup>-6</sup>		
NGC1333-SVS13	Blue	-0.5 → 4.5	0.20 (0.02)	0.53 (0.05)	34.9 ( 3.1)	6.7×10 <sup>-1</sup>	5.1×10 <sup>-7</sup>
		-5.5 → -0.5	0.13 (0.02)	0.34 (0.05)	...	2.6×10 <sup>-2</sup>	5.7×10 <sup>-6</sup>
		-10.5 → -5.5	0.09 (0.02)	0.24 (0.05)	...	5.5×10 <sup>-3</sup>	1.6×10 <sup>-5</sup>
		-15.5 → -10.5	0.12 (0.02)	0.30 (0.05)	...	2.4×10 <sup>-3</sup>	4.8×10 <sup>-5</sup>
		-20.5 → -15.5	< 0.05	< 0.14	...	1.5×10 <sup>-3</sup>	<3.1×10 <sup>-5</sup>
	Red	11.5 → 16.5	0.30 (0.02)	0.79 (0.05)	30.3 ( 1.7)	5.7×10 <sup>-1</sup>	7.2×10 <sup>-7</sup>
		16.5 → 21.5	0.17 (0.02)	0.44 (0.05)	...	4.4×10 <sup>-2</sup>	4.6×10 <sup>-6</sup>
		21.5 → 26.5	0.10 (0.02)	0.27 (0.05)	...	8.7×10 <sup>-3</sup>	1.5×10 <sup>-5</sup>
		26.5 → 31.5	0.07 (0.02)	0.18 (0.05)	...	1.2×10 <sup>-3</sup>	7.9×10 <sup>-5</sup>



Table 3—Continued

Source		$V_{LSR}$ Interval (km s <sup>-1</sup> )	$\int T_A^*(\text{H}_2\text{O})dv$ (K km s <sup>-1</sup> )	H <sub>2</sub> O Line Flux (10 <sup>-20</sup> W cm <sup>-2</sup> )	<sup>12</sup> CO/ <sup>13</sup> CO	Mass (M <sub>⊙</sub> )	o-H <sub>2</sub> O Abundance <sup>b</sup>
Orion KL	Blue	-0.5 → 4.5	10.2 (0.03)	26.92 (0.09)	20.2 ( 0.4)	7.8	2.4×10 <sup>-6</sup>
		-5.5 → -0.5	8.28 (0.03)	21.77 (0.09)	25.1 ( 1.1)	2.2	6.4×10 <sup>-6</sup>
		-10.5 → -5.5	6.30 (0.03)	16.57 (0.09)	34.4 ( 3.1)	1.2	8.1×10 <sup>-6</sup>
		-15.5 → -10.5	4.98 (0.03)	13.11 (0.09)	49.2 ( 9.5)	5.3×10 <sup>-1</sup>	1.3×10 <sup>-5</sup>
		-20.5 → -15.5	3.80 (0.03)	9.99 (0.09)	...	2.6×10 <sup>-1</sup>	1.9×10 <sup>-5</sup>
		-25.5 → -20.5	3.01 (0.03)	7.92 (0.09)	...	1.1×10 <sup>-1</sup>	3.6×10 <sup>-5</sup>
		-30.5 → -25.5	2.26 (0.03)	5.94 (0.09)	...	3.8×10 <sup>-2</sup>	9.2×10 <sup>-5</sup>
	Red	-35.5 → -30.5	1.60 (0.03)	4.21 (0.09)	...	1.8×10 <sup>-2</sup>	1.2×10 <sup>-4</sup>
		13.5 → 18.5	13.7 (0.03)	36.12 (0.09)	24.1 ( 0.5)	6.7	4.3×10 <sup>-6</sup>
		18.5 → 23.5	10.8 (0.03)	28.36 (0.09)	27.2 ( 1.3)	1.8	1.3×10 <sup>-5</sup>
		23.5 → 28.5	8.22 (0.03)	21.61 (0.09)	28.3 ( 2.4)	8.9×10 <sup>-1</sup>	1.8×10 <sup>-5</sup>
		28.5 → 33.5	5.94 (0.03)	15.61 (0.09)	...	2.2×10 <sup>-1</sup>	4.9×10 <sup>-5</sup>
		33.5 → 38.5	3.99 (0.03)	10.50 (0.09)	...	1.1×10 <sup>-1</sup>	6.6×10 <sup>-5</sup>
		38.5 → 43.5	2.61 (0.03)	6.87 (0.09)	...	4.5×10 <sup>-2</sup>	9.6×10 <sup>-5</sup>
OMC2	Blue	43.5 → 48.5	1.70 (0.03)	4.47 (0.09)	...	2.8×10 <sup>-2</sup>	8.5×10 <sup>-5</sup>
		48.5 → 53.5	1.09 (0.03)	2.86 (0.09)	...	2.2×10 <sup>-2</sup>	8.1×10 <sup>-5</sup>
	Red	2.5 → 7.5	0.46 (0.05)	1.22 (0.12)	21.7 ( 1.6)	4.2	1.6×10 <sup>-7</sup>
		-2.5 → 2.5	0.38 (0.05)	0.99 (0.12)	...	1.9×10 <sup>-2</sup>	1.7×10 <sup>-5</sup>
HH25mm	Blue	13.5 → 18.5	0.56 (0.05)	1.46 (0.12)	52.4 ( 9.7)	1.3	5.3×10 <sup>-7</sup>
		18.5 → 23.5	0.27 (0.05)	0.71 (0.12)	...	1.6×10 <sup>-2</sup>	1.3×10 <sup>-5</sup>
		3.5 → 8.5	0.16 (0.02)	0.42 (0.05)	17.8 ( 0.4)	4.8	1.7×10 <sup>-7</sup>
	Red	-1.5 → 3.5	0.12 (0.02)	0.33 (0.05)	...	7.6×10 <sup>-2</sup>	7.0×10 <sup>-6</sup>
		-6.5 → -1.5	0.08 (0.02)	0.21 (0.05)	...	7.8×10 <sup>-3</sup>	3.0×10 <sup>-5</sup>
		12.0 → 17.0	0.19 (0.02)	0.49 (0.05)	26.4 ( 1.1)	3.6	3.0×10 <sup>-7</sup>
		17.0 → 22.0	0.16 (0.02)	0.42 (0.05)	37.3 ( 8.2)	3.1×10 <sup>-1</sup>	3.8×10 <sup>-6</sup>
		22.0 → 27.0	0.09 (0.02)	0.23 (0.05)	...	3.4×10 <sup>-2</sup>	2.7×10 <sup>-5</sup>
NGC2071	Blue	27.0 → 32.0	< 0.06	< 0.16	...	8.2×10 <sup>-3</sup>	<1.0×10 <sup>-4</sup>
		32.0 → 37.0	< 0.06	< 0.16	...	1.3×10 <sup>-3</sup>	<7.2×10 <sup>-4</sup>
1.5 → 6.5	0.35 (0.03)	0.91 (0.07)	20.9 ( 0.4)	6.4	4.2×10 <sup>-8</sup>		

Table 3—Continued

Source	$V_{LSR}$ Interval (km s <sup>-1</sup> )	$\int T_A^*(\text{H}_2\text{O})dv$ (K km s <sup>-1</sup> )	H <sub>2</sub> O Line Flux (10 <sup>-20</sup> W cm <sup>-2</sup> )	<sup>12</sup> CO/ <sup>13</sup> CO	Mass (M <sub>⊙</sub> )	o-H <sub>2</sub> O Abundance <sup>b</sup>
	-3.5 → 1.5	0.29 (0.03)	0.75 (0.07)	31.7 ( 2.0)	8.9×10 <sup>-1</sup>	2.1×10 <sup>-7</sup>
	-8.5 → -3.5	0.17 (0.03)	0.43 (0.07)	...	9.0×10 <sup>-2</sup>	1.1×10 <sup>-6</sup>
	-13.5 → -8.5	< 0.08	< 0.21	...	2.6×10 <sup>-2</sup>	<1.7×10 <sup>-6</sup>
	-18.5 → -13.5	0.16 (0.03)	0.42 (0.07)	...	1.6×10 <sup>-2</sup>	5.5×10 <sup>-6</sup>
	-23.5 → -18.5	< 0.08	< 0.21	...	3.2×10 <sup>-3</sup>	<1.4×10 <sup>-5</sup>
Red	12.5 → 17.5	0.81 (0.03)	2.14 (0.07)	26.4 ( 0.4)	7.2	9.9×10 <sup>-8</sup>
	17.5 → 22.5	0.41 (0.03)	1.09 (0.07)	60.1 ( 9.1)	4.7×10 <sup>-1</sup>	6.1×10 <sup>-7</sup>
	22.5 → 27.5	0.25 (0.03)	0.65 (0.07)	...	8.8×10 <sup>-2</sup>	1.8×10 <sup>-6</sup>
	27.5 → 32.5	0.16 (0.03)	0.42 (0.07)	...	3.2×10 <sup>-2</sup>	3.0×10 <sup>-6</sup>
	32.5 → 37.5	0.10 (0.03)	0.26 (0.07)	...	8.5×10 <sup>-3</sup>	6.6×10 <sup>-6</sup>
MonR2	Blue 2.8 → 7.8	0.38 (0.03)	1.01 (0.07)	9.9 ( 0.1)	1.3×10 <sup>2</sup>	1.5×10 <sup>-8</sup>
	-2.2 → 2.8	0.08 (0.03)	0.22 (0.07)	...	1.4×10 <sup>-1</sup>	2.7×10 <sup>-6</sup>
	Red 13.0 → 18.0	0.45 (0.03)	1.19 (0.07)	8.0 ( 0.0)	2.4×10 <sup>2</sup>	1.1×10 <sup>-8</sup>
	18.0 → 23.0	0.09 (0.03)	0.24 (0.07)	17.9 ( 1.7)	1.3×10 <sup>1</sup>	3.1×10 <sup>-8</sup>
	23.0 → 28.0	< 0.08	< 0.21	...	2.4×10 <sup>-1</sup>	<1.2×10 <sup>-6</sup>
NGC2264 D	Blue -4.0 → 1.0	0.09 (0.02)	0.24 (0.05)	...	1.6	1.1×10 <sup>-6</sup>
	-9.0 → -4.0	< 0.05	< 0.14	...	5.2×10 <sup>-2</sup>	<1.6×10 <sup>-5</sup>
	Red 10.0 → 15.0	0.13 (0.02)	0.35 (0.05)	...	1.8	1.6×10 <sup>-6</sup>
	15.0 → 20.0	0.06 (0.02)	0.16 (0.05)	...	7.5×10 <sup>-2</sup>	2.9×10 <sup>-5</sup>
NGC2264 C	Red 11.0 → 16.0	0.52 (0.03)	1.37 (0.08)	22.1 ( 1.0)	6.3	1.2×10 <sup>-6</sup>
	16.0 → 21.0	0.31 (0.03)	0.80 (0.08)	14.9 ( 4.1)	5.8×10 <sup>-1</sup>	6.4×10 <sup>-6</sup>
ρ Oph A	Blue -3.5 → 1.5	0.28 (0.01)	0.74 (0.04)	17.8 ( 2.7)	2.2×10 <sup>-1</sup>	9.5×10 <sup>-7</sup>
	Red 6.0 → 11.0	0.17 (0.01)	0.43 (0.04)	13.3 ( 1.1)	4.3×10 <sup>-1</sup>	3.7×10 <sup>-7</sup>
L1689N	Blue -2.5 → 2.5	0.37 (0.03)	0.97 (0.07)	18.3 ( 1.8)	2.2×10 <sup>-1</sup>	7.5×10 <sup>-7</sup>
	-7.5 → -2.5	0.13 (0.03)	0.33 (0.07)	...	6.8×10 <sup>-3</sup>	8.4×10 <sup>-6</sup>
	-12.5 → -7.5	< 0.08	< 0.21	...	9.9×10 <sup>-4</sup>	<3.3×10 <sup>-5</sup>
	Red 6.0 → 11.0	0.72 (0.03)	1.89 (0.07)	21.3 ( 2.5)	9.0×10 <sup>-2</sup>	2.5×10 <sup>-6</sup>
	11.0 → 16.0	0.25 (0.03)	0.66 (0.07)	...	4.7×10 <sup>-3</sup>	1.6×10 <sup>-5</sup>

Table 3—Continued

Source		$V_{LSR}$ Interval (km s <sup>-1</sup> )	$\int T_A^*(\text{H}_2\text{O})dv$ (K km s <sup>-1</sup> )	H <sub>2</sub> O Line Flux (10 <sup>-20</sup> W cm <sup>-2</sup> )	<sup>12</sup> CO/ <sup>13</sup> CO	Mass (M <sub>⊙</sub> )	o-H <sub>2</sub> O Abundance <sup>b</sup>
		16.0 → 21.0	0.11 (0.03)	0.29 (0.07)	...	4.9×10 <sup>-4</sup>	8.1×10 <sup>-5</sup>
Ser SMM1	Blue	0.5 → 5.5	0.27 (0.01)	0.70 (0.04)	17.8 ( 0.8)	1.9	4.7×10 <sup>-7</sup>
		-4.5 → 0.5	0.13 (0.01)	0.35 (0.04)	...	1.9×10 <sup>-2</sup>	1.6×10 <sup>-5</sup>
	Red	11.0 → 16.0	0.18 (0.01)	0.48 (0.04)	17.9 ( 0.6)	3.0	2.1×10 <sup>-7</sup>
		16.0 → 21.0	0.14 (0.01)	0.36 (0.04)	...	3.6×10 <sup>-2</sup>	1.4×10 <sup>-5</sup>
L1157	Blue	-3.5 → 1.5	0.33 (0.01)	0.86 (0.04)	35.4 ( 5.6)	2.8×10 <sup>-1</sup>	5.3×10 <sup>-6</sup>
		-8.5 → -3.5	0.22 (0.01)	0.58 (0.04)	...	1.9×10 <sup>-2</sup>	4.9×10 <sup>-5</sup>
		-13.5 → -8.5	0.15 (0.01)	0.40 (0.04)	...	3.9×10 <sup>-3</sup>	3.5×10 <sup>-4</sup>
	Red	4.0 → 9.0	0.23 (0.01)	0.59 (0.04)	33.7 ( 7.0)	2.9×10 <sup>-1</sup>	3.8×10 <sup>-6</sup>
		9.0 → 14.0	0.14 (0.01)	0.37 (0.04)	...	5.2×10 <sup>-2</sup>	1.3×10 <sup>-5</sup>
		14.0 → 19.0	0.11 (0.01)	0.28 (0.04)	...	3.6×10 <sup>-2</sup>	1.5×10 <sup>-5</sup>
		19.0 → 24.0	0.06 (0.01)	0.16 (0.04)	...	2.0×10 <sup>-2</sup>	1.6×10 <sup>-5</sup>
		24.0 → 29.0	0.07 (0.01)	0.18 (0.04)	...	7.0×10 <sup>-3</sup>	5.2×10 <sup>-5</sup>
L1228	Blue	-14.5 → -9.5	0.09 (0.01)	0.24 (0.04)	20.9 ( 1.0)	8.4×10 <sup>-1</sup>	3.2×10 <sup>-7</sup>
		-19.5 → -14.5	0.08 (0.01)	0.22 (0.04)	...	2.2×10 <sup>-2</sup>	1.2×10 <sup>-5</sup>
	Red	-6.0 → -1.0	0.08 (0.01)	0.21 (0.04)	21.1 ( 2.0)	5.1×10 <sup>-1</sup>	4.5×10 <sup>-7</sup>
		-1.0 → 4.0	0.07 (0.01)	0.17 (0.04)	...	5.3×10 <sup>-3</sup>	4.4×10 <sup>-5</sup>
IC1396N	Blue	-8.0 → -3.0	0.17 (0.01)	0.46 (0.04)	30.9 ( 4.4)	1.2	1.6×10 <sup>-6</sup>
		-13.0 → -8.0	0.10 (0.01)	0.27 (0.04)	...	1.1×10 <sup>-1</sup>	1.2×10 <sup>-5</sup>
		-18.0 → -13.0	0.08 (0.01)	0.22 (0.04)	...	1.6×10 <sup>-2</sup>	5.8×10 <sup>-5</sup>
	Red	4.0 → 9.0	0.20 (0.01)	0.52 (0.04)	30.3 ( 4.4)	1.4	1.7×10 <sup>-6</sup>
		9.0 → 14.0	0.10 (0.01)	0.26 (0.04)	...	3.6×10 <sup>-2</sup>	2.6×10 <sup>-5</sup>
		14.0 → 19.0	< 0.04	< 0.11	...	4.5×10 <sup>-3</sup>	<8.5×10 <sup>-5</sup>
S140	Blue	-16.0 → -11.0	0.14 (0.02)	0.37 (0.05)	13.8 ( 0.2)	3.0×10 <sup>1</sup>	1.5×10 <sup>-8</sup>
		-21.0 → -16.0	< 0.05	< 0.14	21.0 ( 1.3)	3.8	<4.1×10 <sup>-8</sup>
		-26.0 → -21.0	< 0.05	< 0.14	...	1.6×10 <sup>-1</sup>	<8.7×10 <sup>-7</sup>
		-31.0 → -26.0	0.09 (0.02)	0.25 (0.05)	...	2.8×10 <sup>-2</sup>	9.0×10 <sup>-6</sup>
		-36.0 → -31.0	< 0.05	< 0.14	...	1.5×10 <sup>-2</sup>	<1.5×10 <sup>-5</sup>

Table 3—Continued

Source	$V_{LSR}$ Interval ( $\text{km s}^{-1}$ )	$\int T_A^*(\text{H}_2\text{O})dv$ ( $\text{K km s}^{-1}$ )	$\text{H}_2\text{O}$ Line Flux ( $10^{-20} \text{ W cm}^{-2}$ )	$^{12}\text{CO}/^{13}\text{CO}$	Mass ( $M_\odot$ )	$\text{o-H}_2\text{O}$ Abundance <sup>b</sup>	
	Red	-4.0 → 1.0	0.42 (0.02)	1.09 (0.05)	17.3 ( 0.5)	$1.5 \times 10^1$	$9.7 \times 10^{-8}$
		1.0 → 6.0	0.06 (0.02)	0.15 (0.05)	...	$4.7 \times 10^{-1}$	$4.9 \times 10^{-7}$
Ceph A HW2	Blue	-20.0 → -15.0	0.62 (0.03)	1.63 (0.08)	12.0 ( 0.2)	$1.9 \times 10^1$	$8.5 \times 10^{-8}$
		-25.0 → -20.0	0.34 (0.03)	0.90 (0.08)	29.0 ( 5.3)	$8.8 \times 10^{-1}$	$8.5 \times 10^{-7}$
		-30.0 → -25.0	0.25 (0.03)	0.65 (0.08)	...	$1.1 \times 10^{-1}$	$4.7 \times 10^{-6}$
		-35.0 → -30.0	0.13 (0.03)	0.35 (0.08)	...	$4.6 \times 10^{-2}$	$5.5 \times 10^{-6}$
	Red	-6.0 → -1.0	0.74 (0.03)	1.94 (0.08)	15.3 ( 0.4)	$1.9 \times 10^1$	$1.1 \times 10^{-7}$
		-1.0 → 4.0	0.40 (0.03)	1.04 (0.08)	...	$4.4 \times 10^{-1}$	$2.1 \times 10^{-6}$
		4.0 → 9.0	< 0.09	< 0.24	...	$3.1 \times 10^{-1}$	$< 8.6 \times 10^{-7}$
	9.0 → 14.0	< 0.09	< 0.24	...	$2.8 \times 10^{-2}$	$< 6.4 \times 10^{-6}$	

<sup>a</sup>The numbers in parantheses are  $1\text{-}\sigma$  statistical uncertainties on the integrated intensity, line flux and observed isotopic ratio. All limits quoted are  $3\text{-}\sigma$

<sup>b</sup> $\text{o-H}_2\text{O}$  abundances relative to  $\text{H}_2$  assuming a  $\text{H}_2/\text{CO}$  ratio of  $10^4$

Table 4. ISO Results

Source	Flux(o-H <sub>2</sub> O 179 $\mu$ m) $10^{-20}$ W cm <sup>-2</sup>	Solid Angle sr	Mass $M_{\odot}$	H <sub>2</sub> O Flux Ratio (179 $\mu$ m/538 $\mu$ m)
L1448-mm	26.9 $\pm$ 3.4 <sup>a</sup>	4.3 $\times 10^{-10}$	4 $\times 10^{-3}$	18.3
NGC1333-SVS13	14.7 $\pm$ 4.1 <sup>b</sup>	1.8 $\times 10^{-10}$	8 $\times 10^{-4}$	4.7
HH25mm	10 $\pm$ 2	1.2 $\times 10^{-10}$	2 $\times 10^{-3}$	4.4
L1689N	21 $\pm$ 2	2.6 $\times 10^{-10}$	3 $\times 10^{-4}$	4.8
Ser SMM1	14.0 $\pm$ 3.2	1.7 $\times 10^{-10}$	2 $\times 10^{-3}$	7.4
L1157	26.5 $\pm$ 3.5 <sup>c</sup>	2.7 $\times 10^{-10}$	5 $\times 10^{-3}$	7.7
Orion KL	2550 $\pm$ 300	3.1 $\times 10^{-8}$	5 $\times 10^{-1}$	10.7

<sup>a</sup>Includes positions L1448-mm and IRS3

<sup>b</sup>Includes positions SVS13 and HH7

<sup>c</sup>Includes positions ON and Blue

Table 5. SWAS CI Abundances<sup>a</sup>

Source		$\int T_A^*([\text{CI}])dv$ (K km s <sup>-1</sup> )	CI Abundance <sup>b</sup>
L1448-mm	Blue	< 0.14	<1.5×10 <sup>-5</sup>
	Red	< 0.10	<2.5×10 <sup>-5</sup>
GL490	Blue	0.49 (0.06)	1.3×10 <sup>-5</sup>
	Red	0.53 (0.06)	1.7×10 <sup>-5</sup>
NGC1333-SVS13	Blue	0.55 (0.05)	3.2×10 <sup>-5</sup>
	Red	< 0.14	<5.7×10 <sup>-6</sup>
Orion KL	Blue	1.16 (0.03)	6.7×10 <sup>-6</sup>
	Red	2.04 (0.03)	1.4×10 <sup>-5</sup>
OMC-2	Blue	< 0.21	<9.7×10 <sup>-6</sup>
	Red	< 0.21	<2.4×10 <sup>-5</sup>
HH25mm	Blue	0.44 (0.04)	1.0×10 <sup>-5</sup>
	Red	0.49 (0.05)	1.3×10 <sup>-5</sup>
NGC2071	Blue	0.49 (0.06)	6.0×10 <sup>-6</sup>
	Red	0.49 (0.06)	6.5×10 <sup>-6</sup>
MonR2	Blue	2.27 (0.05)	1.0×10 <sup>-5</sup>
	Red	3.80 (0.07)	8.9×10 <sup>-6</sup>
NGC2264 D	Blue	0.26 (0.03)	5.9×10 <sup>-5</sup>
	Red	0.29 (0.03)	7.2×10 <sup>-5</sup>
NGC2264 C	Red	< 0.20	<8.5×10 <sup>-6</sup>
$\rho$ Oph A	Blue	0.80 (0.02)	5.5×10 <sup>-5</sup>
	Red	0.83 (0.02)	3.6×10 <sup>-5</sup>
L1689N	Blue	0.27 (0.05)	9.0×10 <sup>-6</sup>
	Red	< 0.15	<8.1×10 <sup>-6</sup>

Table 5—Continued

Source		$\int T_A^*([\text{CI}])dv$ (K km s <sup>-1</sup> )	CI Abundance <sup>b</sup>
Ser SM1	Blue	< 0.12	<4.2×10 <sup>-6</sup>
	Red	0.39 (0.04)	9.0×10 <sup>-6</sup>
L1157	Blue	0.10 (0.03)	2.3×10 <sup>-5</sup>
	Red	0.11 (0.04)	3.4×10 <sup>-5</sup>
L1228	Blue	0.31 (0.02)	2.1×10 <sup>-5</sup>
	Red	0.28 (0.02)	3.3×10 <sup>-5</sup>
IC1396N	Blue	< 0.13	<2.0×10 <sup>-5</sup>
	Red	< 0.13	<2.6×10 <sup>-5</sup>
S140	Blue	0.88 (0.03)	1.0×10 <sup>-5</sup>
	Red	0.37 (0.02)	9.2×10 <sup>-6</sup>
Ceph A HW2	Blue	1.36 (0.04)	2.2×10 <sup>-5</sup>
	Red	1.36 (0.04)	2.3×10 <sup>-5</sup>

<sup>a</sup>The numbers in parantheses are 1- $\sigma$  statistical uncertainties on the integrated intensity, line flux and observed isotopic ratio. All limits quoted are 3- $\sigma$

<sup>b</sup>CI abundances relative to H<sub>2</sub> assuming a H<sub>2</sub>/CO ratio of 10<sup>4</sup>

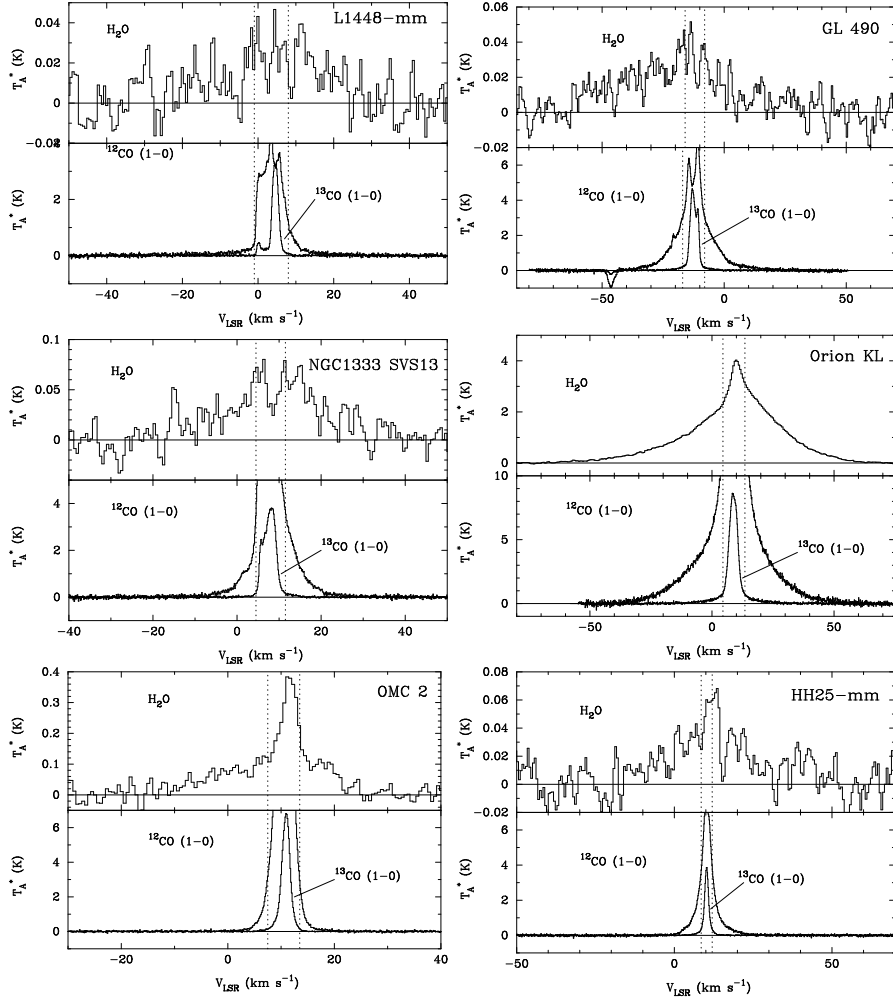


Fig. 1.— (a) Spectra towards L1448-mm, GL490, NGC1333-SVS13, OMC 1, OMC 2 and HH25-mm. The positions observed are provided in Table 1. For each source there are two panels, the upper panel shows the spectrum of the  $1_{10} \rightarrow 1_{01}$  transition of ortho-H<sub>2</sub>O



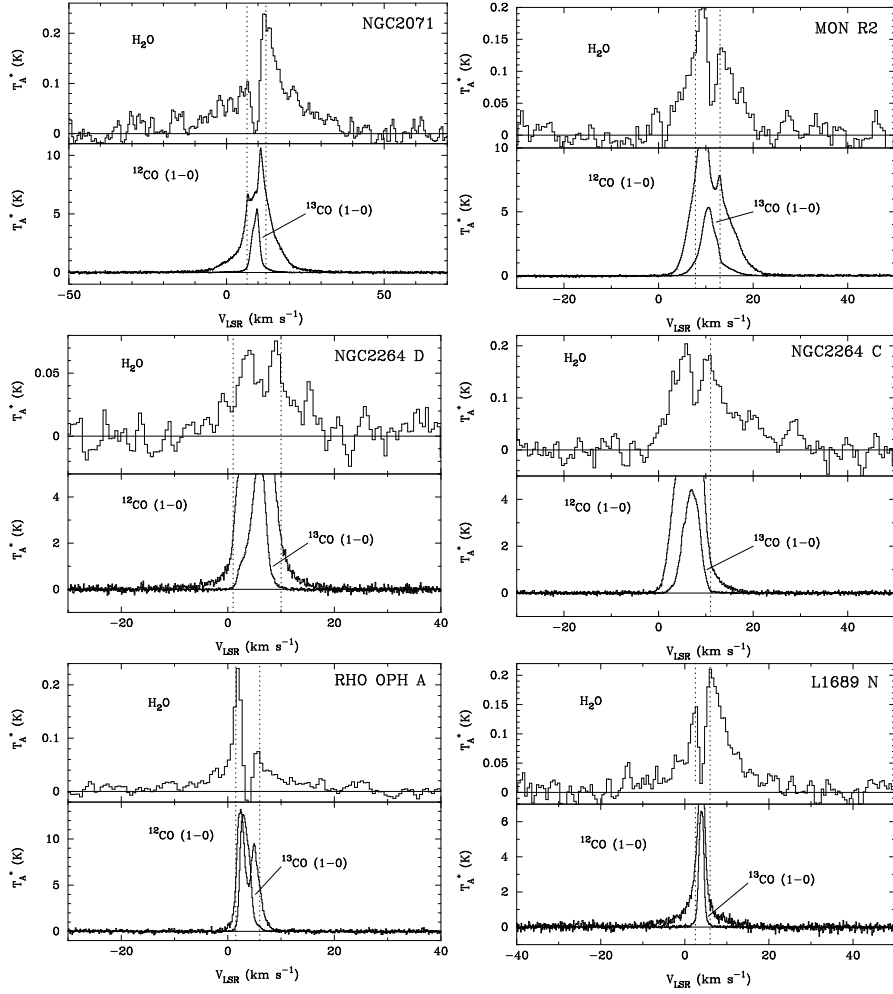


Fig. 1.— (b) The same as Fig. 1a for NGC2071, MonR2, NGC2264 D, NGC2264 C,  $\rho$  Oph A, and L1689 N.

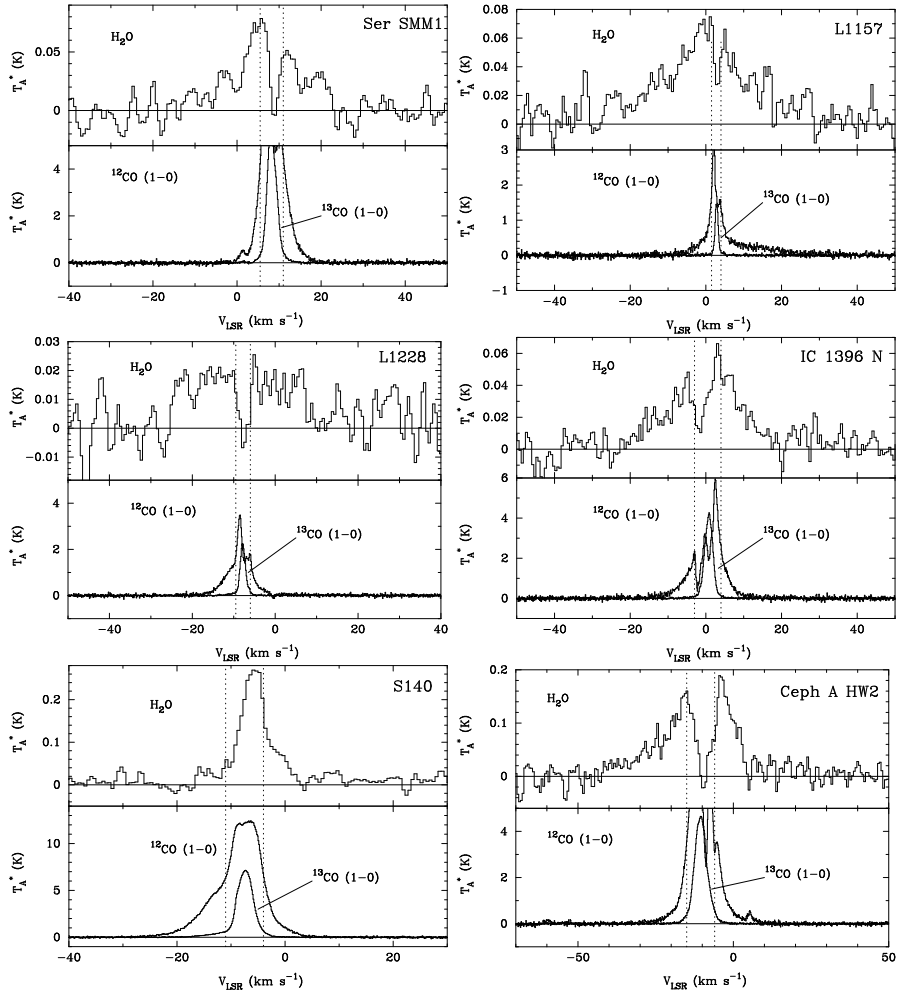


Fig. 1.— (c) The same as Fig. 1a for Ser SMM1, L1157, L1228, IC 1396N, S140 and Ceph A HW2.

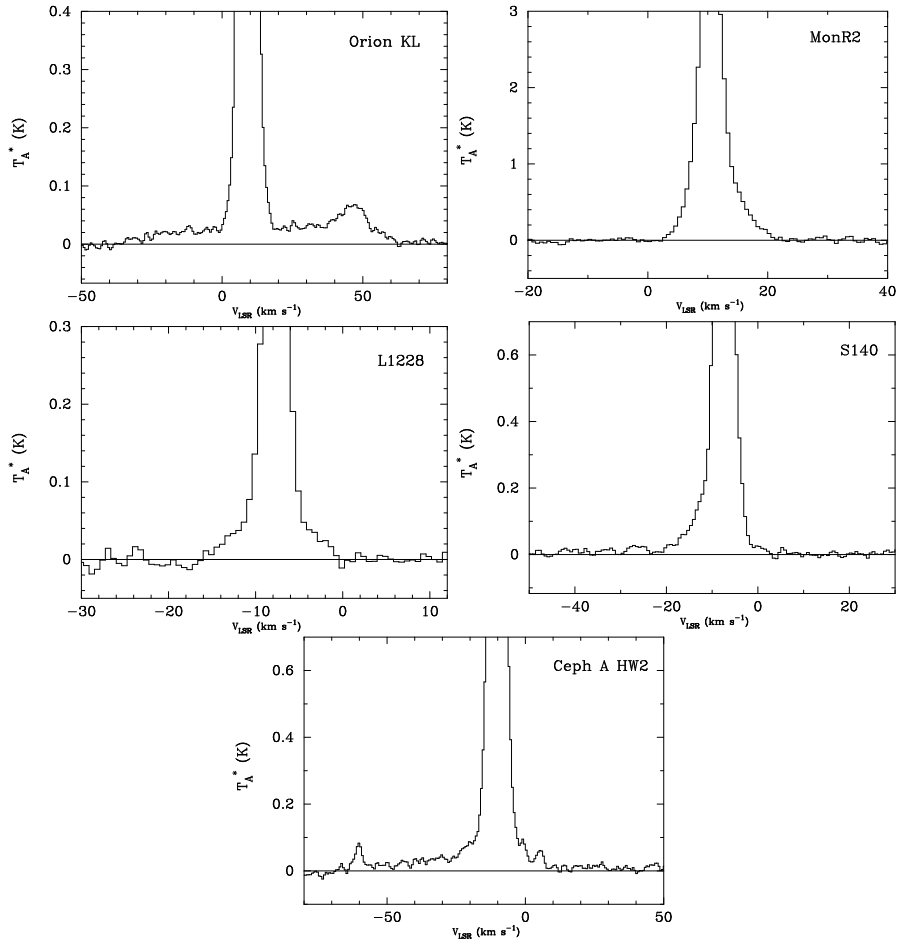


Fig. 2.— Spectra of the  $^3P_1 \rightarrow ^3P_0$  transition of [CI] towards OMC 1, Mon R2, L1228, S140 and Ceph A HW2 obtained with SWAS. The positions observed are provided in Table 1.